Research article

JGS
Journal of the Geological Society

Published online March 28, 2019

https://doi.org/10.1144/jgs2018-162 | Vol. 176 | 2019 | pp. 704–726

Exhumation history of the Aydın range and the role of the Büyük Menderes detachment system during bivergent extension of the central Menderes Massif, western Turkey

Nils-Peter Nilius[1*], Christoph Glotzbach[2], Andreas Wölfler[1], Andrea Hampel[1], István Dunkl[3], Cüneyt Akal[4], Caroline Heineke[5] & Ralf Hetzel[5]

[1] Institute of Geology, Leibniz University of Hannover, Callinstraße 30, 30167 Hannover, Germany
[2] Department of Geosciences, University of Tübingen, Wilhelmstraße 56, 72074 Tübingen, Germany
[3] University of Göttingen, Geoscience Center, Sedimentology and Environment Geology, Goldschmidstraße 3, 37077 Göttingen, Germany
[4] Engineering Faculty, Department of Geological Engineering, Tınaztepe Campus, Buca, 35390 Izmir, Turkey
[5] Institute of Geology and Palaeontology, University of Münster, Correnssstraße 24, 48149 Münster, Germany
N-PN, 0000-0002-3936-6507
* Correspondence: nilius@geowi.uni-hannover.de

Abstract: The central Menderes Massif (western Turkey) is a prominent example of symmetrical exhumation of a core complex. It comprises the Bozdağ and Aydın ranges, which represent the footwalls of the north-dipping Gediz detachment and the south-dipping Büyük Menderes detachment, respectively. In contrast to the Gediz detachment, the role of the Büyük Menderes detachment during Late Cenozoic extension and exhumation of the central Menderes Massif is less well resolved. Here, we present results from structural and geological mapping as well as new fission-track and (U–Th)/He data to show that two low-angle normal faults contributed to the exhumation of the Aydın range. Our data indicate that the sustained activity of the Büyük Menderes detachment since the early Miocene is followed by the onset of faulting along the previously unrecognized Demirhan detachment, which is situated in the hanging wall of the Büyük Menderes detachment, in the latest Miocene/Pliocene. Thermokinematic modelling of cooling ages from the footwalls of the Büyük Menderes and Demirhan detachments yielded exhumation rates of *c.* 0.5 and *c.* 0.4 km Ma^{-1}, respectively. Apatite fission track ages from the Demirhan detachment indicate a slip rate of *c.* 2 km Ma^{-1} during the Pliocene. High-angle normal faulting along the modern Büyük Menderes graben commenced in the Quaternary.

Supplementary material: Further results of thermal history modelling are available at https://doi.org/10.6084/m9.figshare.c.4392905

Low-angle normal faults accommodate large-scale crustal extension and have been observed in different tectonic environments, for example, in backarc (e.g. Jolivet & Brun 2010; Ustaszewski *et al.* 2010), post-orogenic (Wernicke 1992; Malavieille 1993) and syn-orogenic (e.g. Lister & Davis 1989; Burchfiel *et al.* 1992; Lee & Lister 1992; Campani *et al.* 2010; Rutte *et al.* 2017) settings. These field observations were complemented by numerical and analogue models, which identified two endmember models that are either dominated by pure shear strain, where bivergent extension leads to symmetrical exhumation (McKenzie 1978), or by asymmetrical simple shear strain (Wernicke 1985). A combination of both models has also been proposed (e.g. Lister *et al.* 1986). However, most natural examples of core complexes have been exhumed in an asymmetrical manner (Brun *et al.* 2017*a*, *b*), i.e. a single low-angle normal fault accommodates most of the regional extension. Rare examples of symmetrically exhumed core complexes occur in western Turkey (Bozkurt 2000; Gessner *et al.* 2001*a*; Ring *et al.* 2003) and in the Aegean region (Grasemann *et al.* 2012) (Fig. 1).

In the Aegean region and western Turkey, large-scale continental extension commenced after Alpine nappe stacking had ceased in the Eocene and was attributed to the collapse of the overthickened crust or to the acceleration of the retreating Aegean slab or to a combination of both processes (e.g. Jolivet & Brun 2010; Ersoy *et al.* 2017). Subsequently, vertical thinning of the crust was accommodated by low-angle normal faults leading to the formation of several core complexes, such as the Attic–Cycladic Complex in the Aegean (e.g. Lister *et al.* 1984; Jolivet & Patriat 1999; Huet *et al.* 2009; Jolivet *et al.* 2010) and the Menderes Massif in western Turkey (e.g. Hetzel *et al.* 1995*a*, *b*; Işik & Tekeli 2001; Ring *et al.* 2003; Bozkurt & Sözbilir 2004; Gessner *et al.* 2013). Many models of the Miocene backarc tectonics in the Aegean attribute the thinning of the crust to top-to-the north shearing along the North Cycladic detachment system, implying an asymmetrical mode of extension accommodated by a single detachment fault (Lee & Lister 1992; Vanderhaeghe 2004; Huet *et al.* 2009). However, recent studies in the southern and western Cyclades proposed that top-to-the north shearing observed in the North Cycladic detachment system was accompanied by top-to-the south shearing along the South and West Cycladic detachment systems, implying a more symmetrical bivergent mode of crustal extension (Iglseder *et al.* 2011; Grasemann *et al.* 2012). The study of these detachment systems is, however, hindered by the fact that large areas are located below sea level. To investigate the nature of bivergent continental extension, we focus on the well-exposed central Menderes Massif in western Turkey where bivergent post-orogenic extension was first described by Hetzel *et al.* (1995*b*) (Fig. 1).

The Menderes Massif was exhumed in two stages. The first stage has been attributed to the exhumation of the northern Menderes Massif along the Simav detachment (Fig. 1) in the latest Oligocene to early Miocene (Işik & Tekeli 2001; Ring & Collins 2005; Thomson & Ring 2006; Erkül 2009) and the second stage to the exhumation of the central Menderes Massif since the middle

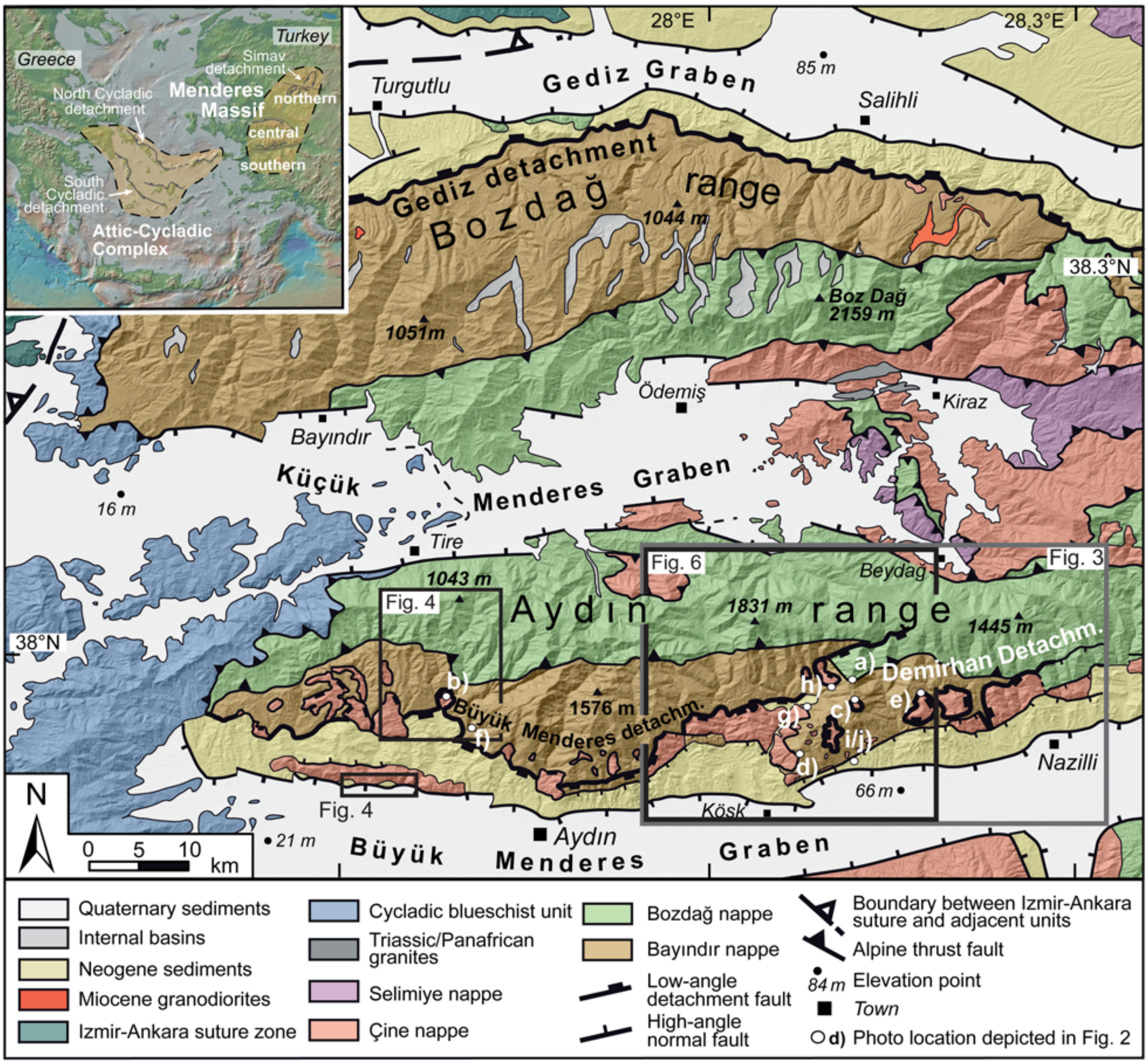

Fig. 1. Geological map of the central Menderes Massif with rectangles outlining the area shown in Figs 3, 4 and 6 (modified from Wölfler *et al.* (2017) and complemented with own field observations). The locations of the photographs in Figure 2 are also indicated.

Miocene (Hetzel *et al.* 1995*a*, *b*; Emre & Sözbilir 1997; Gessner *et al.* 2001*b*). Interestingly, the mode of exhumation of the two sub-massifs is very different, as the northern Menderes Massif was asymmetrically exhumed by top-to-the north faulting on the Simav detachment, whereas the central Menderes Massif was symmetrically exhumed along two oppositely dipping low-angle detachment faults (Hetzel *et al.* 1995*b*; Bozkurt 2001; Ring *et al.* 2003). During this bivergent extension, the north-dipping Gediz detachment exhumed the Bozdağ range, whereas the south-dipping Büyük Menderes detachment exhumed the Aydın range (Figs 1 and 2a, b). The proposed symmetrical exhumation history of the central Menderes Massif is mainly based on temporal and structural constraints derived from the Gediz detachment as it was inferred by the symmetrical architecture of the central Menderes Massif that the Aydın and the Bozdağ range share the same exhumation history (Gessner *et al.* 2001*b*). Consequently, the extensional history of the northern part of the central Menderes Massif is well constrained by geochronological data from the Bozdağ range, which indicate two phases of increased footwall cooling in the middle Miocene and since the latest Miocene/Pliocene by using $^{206}Pb/^{238}U$ dating of monazite and titanite (Glodny & Hetzel 2007; Rossetti *et al.* 2017) as well as low-temperature thermochronology (Hetzel *et al.* 1995*a*; Gessner *et al.* 2001*a*; Ring *et al.* 2003; Buscher *et al.* 2013; Asti *et al.* 2018).

Thermochronological data of Wölfler *et al.* (2017) provided support for the interpretation that the proposed two-stage model of extension and footwall cooling in the middle Miocene and latest Miocene/Pliocene also applies to the Büyük Menderes detachment. However, most other studies from the southern central Menderes Massif focused on the evolution of the Büyük Menderes graben, which is situated in the hanging wall and south of the Büyük Menderes detachment (Sözbilir & Emre 1990; Cohen *et al.* 1995; Bozkurt 2001; Gürer *et al.* 2009; Sen & Seyitoğlu 2009). Nevertheless, the exact age of the Büyük Menderes graben is still disputed and either described as early Miocene to middle Miocene (Sözbilir & Emre 1990; Cohen *et al.* 1995; Akgün & Akyol 1999; Sen & Seyitoğlu 2009) or as latest Miocene/Pliocene (Gürer *et al.* 2009; Ring *et al.* 2017). Additionally, a prevailing extensional tectonic setting during graben formation in the Miocene has been questioned by Gürer *et al.* (2009).

Here we aim to investigate the exhumation history of the central Menderes Massif by focusing on the Aydın range as the footwall of the Büyük Menderes detachment. We have conducted field mapping of major structures related to late Cenozoic extension

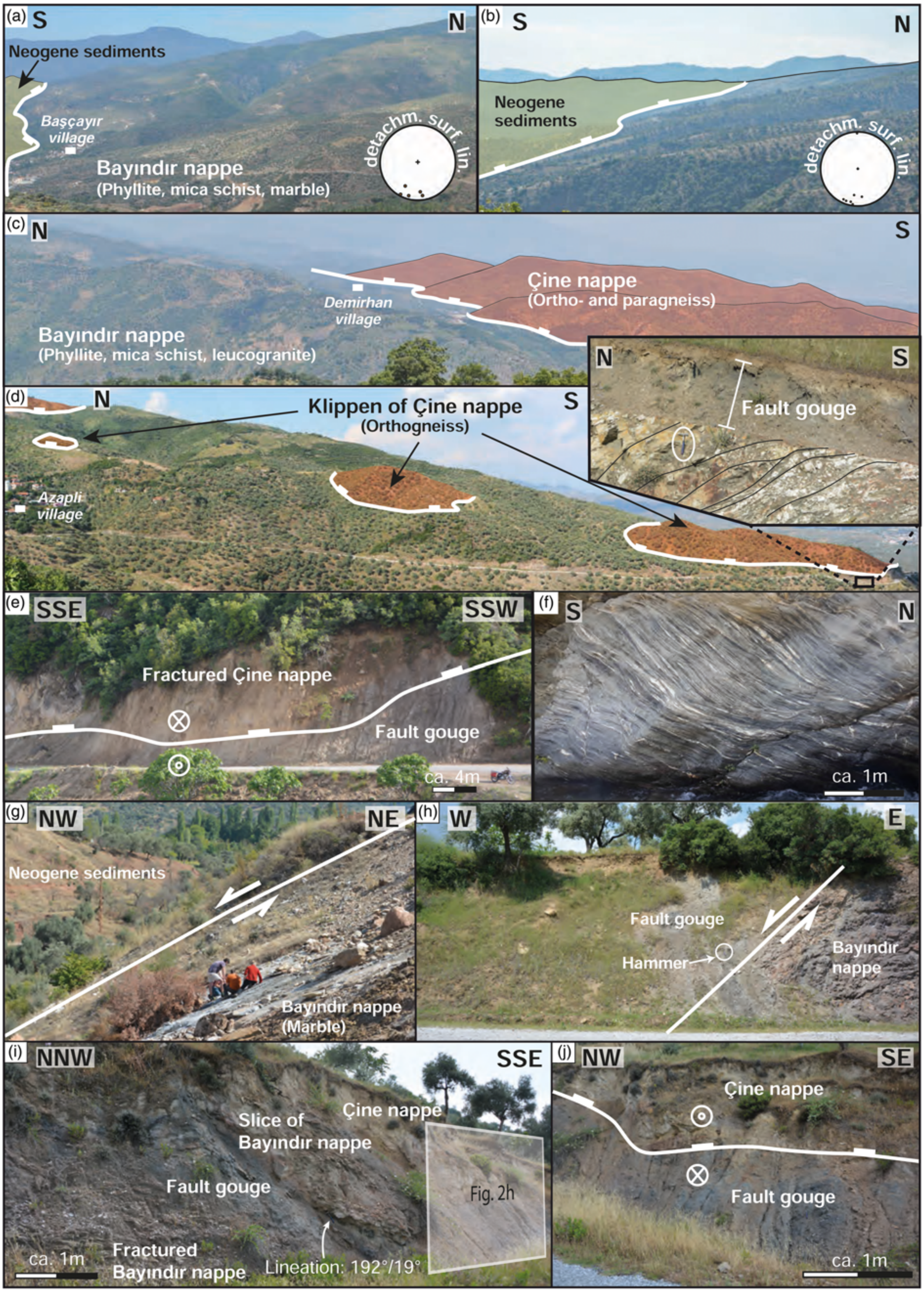

Fig. 2. (**a**) South-dipping footwall of the Büyük Menderes detachment at Başçayır village. (**b**) Erosion resistant footwall of the Büyük Menderes detachment west of Beyköy. (**c**) View to the SE on the southern flank of the Aydın range and the Demirhan detachment. (**d**) Orthogneiss of the hanging wall of the Demirhan detachment south of Karatepe. (**e**) A thick fault gouge horizon between Bayındır nappe and Çine nappe marks the Demirhan detachment west of Demirhan village. (**f**) Mylonitic footwall below the Büyük Menderes detachment near Beyköy. (**g**) Exposure of the WNW-dipping normal fault west of Başçayır village. (**h**) Outcrop of the same normal fault further north, comprising Çine nappe gneisses in the hanging wall and phyllites of the Bayındır nappe in the footwall. (**i**) Exposure of the Demirhan detachment in the uplifted part of the Büyük Menderes Graben north of Nysa. (**j**) Upper limit of the Demirhan detachment fault zone where Çine nappe of the hanging wall rests on fault gouge horizon of the Demirhan detachment. See Figure 1 for locations.

and applied low-temperature thermochronology to detect along-strike changes in the cooling history as well as thermokinematic modelling to obtain exhumation rates. Based on these new structural and thermochronological data, we suggest a new tectonic model for the evolution of the Büyük Menderes graben and improve the constraints on the bivergent exhumation of the central Menderes Massif.

Geological setting of western Turkey

The geological evolution of western Anatolia has been dominated (1) by the convergence between Africa and Eurasia since the middle Cretaceous, which led to the formation of the Anatolides in the Eocene (Şengör & Yilmaz 1981; Candan *et al.* 2005; Kaymakci *et al.* 2009; Jolivet & Brun 2010), and (2) by the ongoing continental extension since the late Oligocene/early Miocene, due to the roll-back of the Hellenic trench (e.g. Gessner *et al.* 2013; Jolivet *et al.* 2013). The proposed crustal architecture of the Menderes Massif is based on geological observations in the southern part of the Menderes Massif and the subdivision between a 'core', consisting of Precambrian metagranites and an overlying 'cover' with Paleozoic/Mesozoic sedimentary units. The sedimentary units are (from bottom to top) composed of amphibolite-facies mica schists, greenschist-facies phyllites and marbles (Schuiling 1962). This core-cover concept was challenged by Bozkurt *et al.* (1993) and revised by Ring *et al.* (1999), who proposed that the Menderes Massif represents an Alpine nappe stack. The main argument against the core-cover concept is the observation that in the central part of the Menderes Massif, the structurally lowest position is occupied by a greenschist-facies metasedimentary unit of late Cretaceous age, which is overlain by older, amphibolite-facies garnet-mica schists and metabasites (Özer & Sözbilir 2003; Gessner *et al.* 2013).

The nappe pile consists of four nappes, with the Bayındır nappe in the lowest position (Ring *et al.* 1999; Gessner *et al.* 2001*c*). Most of the Bayındır nappe is composed of phyllites with intercalated marbles, quartzites and greenschist. The lack of biotite implies a lower greenschist-facies metamorphic overprint with temperatures below 400°C in the late Eocene, with the timing being still poorly constrained by a single $^{40}Ar/^{39}Ar$ white mica age of 36 ± 2 Ma (Lips *et al.* 2001). A rudist-bearing marble unit implies that the Bayındır nappe only experienced one Alpine metamorphic overprint and that the contact to the overlaying Bozdağ nappe must therefore be an Alpine thrust. The metasedimentary units of the Bozdağ nappe experienced amphibolites-facies metamorphic conditions during the Pan-African Orogeny (Candan *et al.* 2001; Ring *et al.* 2001; Koralay 2015). Lithologies constituting the Bozdağ nappe include mainly metapelite and minor volumes of amphibolite, dolomite, eclogite and granitic intrusions of Triassic age (Koralay *et al.* 2001, 2011). As these intrusions also penetrate the Çine nappe above, a pre-Triassic – most probably Pan-African – age for the tectonic contact between Bozdağ and Çine nappe seems likely (Gessner *et al.* 2001*c*). The most prominent lithologies of the Çine nappe are deformed orthogneisses (augengneiss) and minor amounts of orthogneiss, pelitic gneiss, amphibolite and eclogite (Oberhänsli *et al.* 1997). The protoliths of the orthogneisses were calc-alkaline leucogranites, which comprise late Neoproterozoic to early Cambrian intrusion ages (Bozkurt *et al.* 1995; Hetzel & Reischmann 1996; Loos & Reischmann 1999). The uppermost nappe of the Menderes Massif is the Selimiye nappe, which was affected by alpine Barrovian-type metamorphism between 43 and 34 Ma and was thrust over the Çine nappe during the Eocene (Ring *et al.* 2003; Schmidt *et al.* 2015). It consists of metapelites, marbles and metabasites of Paleozoic age (Regnier *et al.* 2003; Gessner *et al.* 2004). The Menderes nappes are overlain by remnants of the Neotethyan ocean; these remnants experienced high-pressure metamorphism during Alpine northward subduction below the Sakarya microcontinent and are exposed north and NW of the central Menderes Massif (Okay & Tüysüz 1999).

Neogene to Recent extension of the Menderes Massif (western Turkey)

In the late Oligocene/early Miocene, the Alpine nappe stack experienced a sustained change to continental extension, leading to low-angle normal faulting and the formation of east–west-striking graben systems, which separate the Menderes Massif into three submassifs. The northern Menderes Massif is separated from the central Menderes Massif by the Gediz graben, and the central Menderes Massif is separated from the southern Menderes Massif by the Büyük Menderes graben (Fig. 1).

The first phase of post-orogenic extension in the Menderes Massif occurred between the late Oligocene to early Miocene, as revealed by apatite and zircon (U–Th)/He and fission track thermochronology as well as by U–Pb ages from syntectonic intrusions. This extension phase is recorded in the northern and southern Menderes Massif, but also in the structurally higher units of the central Menderes Massif (Gessner *et al.* 2001*a*; Ring & Collins 2005; Thomson & Ring 2006; Hasözbek *et al.* 2011; Buscher *et al.* 2013). Only in the northern Menderes Massif can this cooling event be unequivocally attributed to tectonic denudation along the top-to-the-north movement on the Simav detachment (Işik & Tekeli 2001; Işik *et al.* 2004; Thomson & Ring 2006; Erkül 2010).

The second phase of extension is connected to the exhumation of the central Menderes Massif along two extensional detachments with opposite dip (Fig. 1): the Gediz detachment in the north (also called the Alaşehir or Kuzey detachment) (Hetzel *et al.* 1995*a*, *b*; Gessner *et al.* 2001*a*; Seyitoğlu *et al.* 2002; Bozkurt & Sözbilir 2004; Buscher *et al.* 2013) and the Büyük Menderes detachment in the south (also described as the Güney detachment) (Emre & Sözbilir 1997; Bozkurt 2000). The Gediz detachment and the Büyük Menderes detachment are exposed along the Bozdağ and Aydın mountain ranges, respectively, and are separated by the Küçük Menderes Graben (Fig. 1). In the footwall of both detachments, the Bayındır nappe, as the structurally deepest unit of the Alpine nappe pile, constitutes large parts of the cataclastically overprinted footwalls, which are discordantly overlain by Neogene syn-extensional sediments and klippen of Çine nappe augengneiss (e.g. Cohen *et al.* 1995; Sen & Seyitoğlu 2009; Çiftçi & Bozkurt 2010).

The extensional history of the Bozdağ range is well constrained by age data from two granodioritic intrusions (the Turgutlu and Salihli granodiorites). The intrusion of the Salihli granodiorite into the footwall of the Gediz detachment occurred at *c.* 16 Ma and the recrystallization of titanite from mylonitic parts of the granodiorite at 14–15 Ma (U–(Th)–Pb dating) is interpreted to reflect the onset of ductile shearing (Hetzel *et al.* 1995*a*; Glodny & Hetzel 2007; Catlos *et al.* 2010; Rossetti *et al.* 2017) Subsequent cooling and exhumation of the footwall of the Gediz detachment is documented by $^{40}Ar/^{39}Ar$ ages from biotite, yielding an age of *c.* 12 Ma (Hetzel *et al* 1995*a*), and final exhumation during the Pliocene constrained by (U–Th)/He and fission track thermochronology of zircon and apatite (Gessner *et al.* 2001*a*; Ring *et al.* 2003; Buscher *et al.* 2013). Faulting along the Gediz detachment was followed by the onset of high-angle normal faulting at the southern margin of the modern Gediz graben in the late Pliocene (Oner & Dilek 2011; Buscher *et al.* 2013).

The Büyük Menderes detachment was first mapped by Candan *et al.* (1992) and later recognized as an extensional detachment fault with a top-to-the south sense of movement (Emre & Sözbilir 1997). It is exposed along the southern flank of the Aydın range and dips

5–20° to the south. First constraints on the cooling history of the Aydın range in the footwall of the Büyük Menderes detachment were given by a limited set of apatite fission track ages ranging from 16 to 6 Ma (Gessner *et al.* 2001*a*; Ring *et al.* 2003). Wölfler *et al.* (2017) presented thermochronological data along a north–south transect across the Aydın range and identified two episodes of enhanced cooling along the Büyük Menderes detachment. Their dataset implied increased exhumation rates of *c.* 0.9 km Ma^{-1} in the middle Miocene and of *c.* 0.4 km Ma^{-1} in the latest Miocene/Pliocene. This two-phase evolution is also observed in the sedimentary succession of the Büyük Menderes graben, which can be divided into a lower part comprising deformed Miocene sediments and discordantly overlaying undeformed Pliocene to Pleistocene units. The succession starts with the Hasköy formation, which is characterized by fluvio-lacustrine sediments including boulder conglomerates, sandstones and mudstones that contain lignite layers (Sözbilir & Emre 1990). The depositional ages suggested for the Hasköy formation range from early-middle Miocene to late Miocene ages (Sözbilir & Emre 1990; Seyitoğlu & Scott 1991, 1992; Akgün & Akyol 1999). The Hasköy formation is in a conformable contact with the overlying middle Miocene Gökkırantepe formation, consisting exclusively of terrestrial fluvial and alluvial sediments, whereas the boundary to the topmost late Pliocene to Pleistocene Asartepe formation is marked by an unconformity (Sözbilir & Emre 1990; Sen & Seyitoğlu 2009).

Methods

We use zircon and apatite (U–Th)/He (ZHe and AHe) and fission track (ZFT and AFT) thermochronology to derive the post-orogenic thermal history and, in combination with thermokinematic modelling, the exhumation history of the Aydın range (Table 1). The closure temperature of each system refers to a specific temperature through which the sample cooled at the measured time (the cooling age), under the assumption that the cooling path was continuous (Dodson 1973). The samples from the Büyük Menderes and Demirhan detachments were collected from hanging-wall units and in the footwall parallel to the direction of tectonic transport.

Zircon and apatite fission-track analysis

Among the total of 24 samples collected, 20 samples were used for AFT analysis and four were used for ZFT analysis (Table 1). Typical closure temperatures for the ZFT method are *c.* 240°C and for the AFT method *c.* 110°C, even though the exact closure temperature of each system may vary by different factors such as the cooling rate, mineral chemistry and radiation damage (e.g. Dodson 1973; Gleadow & Duddy 1981; Wagner & van den Haute 1992; Rahn *et al.* 2004; Ketcham *et al.* 2007). The temperature ranges from annealing to total resetting of fission tracks are *c.* 190–*c.* 380°C in zircon and *c.* 60–*c.* 120°C for apatite (Green *et al.* 1986; Wagner & van den Haute 1992; Rahn *et al.* 2004).

Conventional magnetic and heavy liquid separation techniques were applied for zircon and apatite separation. Subsequently, the zircon and apatite separates were embedded in PDA TeflonTM and epoxy, respectively, and finally grounded and polished. Zircon mounts were etched in a KOH–NaOH eutectic melt at 215°C (Zaun & Wagner 1985), whereas apatite mounts were etched with 5 M HNO_3 for 20 s at 21°C. We used the external detector method (Gleadow 1981) with uranium-free muscovite sheets and Durango apatite and Fish Canyon zircon age standards for the zeta calibration approach (e.g. Naeser 1978; Hurford & Green 1983). The required irradiation of the samples with thermal neutrons was performed at the FRM-II reactor facility in Garching (Technical University Munich, Germany). To monitor the neutron fluence IRMM-540R and IRMM-541 dosimeter glasses were used. Fission-track counting was carried out with an Olympus BX-51 microscope with 1000× magnification at the Institute of Geology in Hannover. For the assessment of fission track annealing kinetics in apatite we used Dpar values (mean diameter of etch figures on prismatic surfaces of apatite parallel to the crystallographic *c*-axis) (Burtner *et al.* 1994). Fission-track ages were calculated with the TRACKKEY software version 4.2 (Dunkl 2002) and are reported in Tables 2 and 3 with 1σ standard errors. We are unable to report

Table 1. *Location, lithology, and structural position of samples for low-temperature thermochronology*

Sample	Latitude (°N) (WGS 84)	Longitude (°E) (WGS 84)	Elevation (m)	Lithology	Structural position	Thermochronometers applied
15M42	37.88020	27.72991	126	Augengneiss	Çine nappe	AHe, AFT
15M44	37.96619	28.11728	970	Mica schist	Bayındır nappe, footwall	AHe, AFT, ZHe
15M45	38.02442	28.13655	1800	Mica schist	Bayındır nappe, footwall	AFT, ZFT
15M46	38.02466	28.10558	1272	Mica schist	Bayındır nappe, footwall	AHe, AFT, ZHe
15M47	38.02466	28.10558	1272	Mica schist	Bayındır nappe, footwall	AFT, ZHe, ZFT
15M48	38.00683	28.11189	922	Mica schist	Bayındır nappe, footwall	AFT
15M49	37.99857	28.10446	805	Mica schist	Bayındır nappe, footwall	AFT
15M51	37.96117	28.08538	387	Sandstone	Miocene sediments, hanging wall	AHe, AFT
15M52	38.04412	27.75315	1014	Mica schist	Bayındır nappe, footwall	AFT
15M54	38.01768	27.74109	909	Mica schist	Bozdağ nappe, footwall	AFT
15M55	38.00243	27.75802	812	Mica schist	Bozdağ nappe, footwall	AFT, ZHe
15M56	37.98357	27.76323	715	Mica schist	Bayındır nappe, footwall	AFT, ZHe
15M57	37.96844	27.76144	505	Paragneiss	Bayındır nappe, footwall	AFT, ZHe, ZFT
15M58	37.95739	27.75863	292	Mica schist	Bayındır nappe, footwall	AFT, ZHe
15M59	37.94882	27.75504	190	Paragneiss	Çine nappe, hanging wall	AHe, AFT, ZHe, ZFT
16M86	37.89713	27.62427	147	Augengneiss	Çine nappe	AHe, AFT
16M87	37.98260	28.13009	1345	Mica schist	Bozdağ nappe, footwall	AFT, ZHe
16M88	38.00618	28.13879	1226	Paragneiss	Bozdağ nappe, footwall	AFT
16M89	38.02486	28.06677	1652	Orthogneiss	Bozdağ nappe, footwall	AFT, ZHe
16M90	38.00476	28.13803	1255	Paragneiss	Bozdağ nappe, footwall	AFT, ZHe
16M91	38.00623	28.14016	1207	Paragneiss	Bozdağ nappe, footwall	ZHe
16M94	37.95898	27.75963	325	Phyllite	Bayındır nappe, footwall	AFT
16M95	38.00100	27.81659	1186	Paragneiss	Bozdağ nappe, footwall	AFT, ZHe
16M97	37.96945	27.79044	694	Mica schist	Bayındır nappe, footwall	AFT

Table 2. *Results of apatite fission-track analyses*

Sample	Number of grains	ρ_s	N_s	ρ_i	N_i	ρ_d	N_d	$P(\chi^2)$ (%)	Dispersion (%)	Central age±1σ (Ma)	U (ppm)	Dpar (µm)
15M42	17	1.016	37	3.956	144	5.5313	2796	99	0	16.1 ± 3.1	9	2.86
15M44	25	0.919	44	9.562	458	5.5103	2796	96	2	6.0 ± 1.0	26	1.36
15M45	25	3.211	122	22.105	840	5.4794	2796	64	2	9.0 ± 1.0	53	2.99
15M46*	20	3.907	53	19.388	263	5.448	2796	99	0	14.0 ± 2.2	46	1.59
15M47*	10	2.480	31	13.360	167	5.4174	2796	97	0	11.4 ± 2.3	30	2.39
15M48*	21	1.298	27	2.740	57	2.1489	2796	100	0	13.0 ± 3.1	19	1.95
15M49	21	1.507	52	7.072	244	5.3554	2796	92	18	13.3 ± 2.3	28	2.09
15M51	9	4.956	56	19.292	218	5.2934	2796	26	22	15.7 ± 2.8	58	2.39
15M52	22	3.215	79	22.543	554	7.4810	2481	100	0	12.1 ± 1.6	42	1.90
15M54	13	2.331	38	10.061	164	5.2315	2796	81	2	13.2 ± 2.6	27	2.52
15M55	17	1.641	42	8.828	226	5.2005	2796	100	0	11.0 ± 2.0	25	2.14
15M56	25	1.748	54	7.540	233	5.2005	2796	96	0	15.4 ± 2.4	21	1.81
15M57*	8	1.383	13	7.234	68	5.1285	2796	99	0	10.6 ± 3.3	20	1.99
15M58	22	1.546	45	21.306	620	5.1075	2796	80	16	4.3 ± 0.7	58	2.34
15M59	23	1.701	83	12.193	595	4.7896	2796	28	15	7.9 ± 1.3	33	1.87
16M86	20	1.763	35	5.899	137	7.185	2481	99	0	23.5 ± 4.5	13	2.08
16M87	24	3.433	110	23.061	739	7.2356	2481	78	16	12.2 ± 1.5	43	1.52
16M88	17	1.522	63	9.859	408	6.9901	2481	97	0	12.2 ± 1.8	32	1.36
16M89	17	3.513	67	18.091	345	6.9411	2481	99	0	15.3 ± 2.2	34	1.68
16M90	35	3.929	163	23.769	986	6.8920	2481	99	0	12.9 ± 1.3	48	1.86
16M94	23	1.484	42	18.297	518	6.6956	2481	100	0	6.2 ± 1.1	37	1.22
16M95	14	2.479	29	14.276	167	6.6465	2481	100	0	13.1 ± 2.8	35	1.51
16M97	7	1.538	13	11.947	101	6.5975	2481	98	0	9.6 ± 2.9	35	1.60

ρ_s (ρ_i) is the spontaneous (induced) track density (10^5 tracks per cm^2); N_s (N_i) is the number of counted spontaneous (induced) tracks; ρ_d is the dosimeter track density (10^5 tracks per cm^2); N_d is the number of tracks counted on the dosimeter; $P(\chi^2)$ is the probability of obtaining a Chi-square value (χ^2) for n degree of freedom (where n is the number of crystals minus 1); ages were calculated using the zeta calibration method (Hurford & Green 1983), glass dosimeter IRMM540, and zeta values of 226 ± 13 a cm^{-2} (samples without asterisk) and 255 ± 9 a cm^{-2} (samples with asterisk) calculated with Durango apatite standards.

track length measurements, because the apatite do not have a sufficient number of tracks owing to their low uranium content and the young cooling history of the rocks. Nevertheless, the available AFT track length data provided by Wölfler *et al.* (2017) are incorporated in our interpretation.

Zircon and apatite (U–Th)/He analysis

Zircon and apatite (U–Th)/He thermochronology (ZHe, AHe) is based on the accumulation of radiogenic helium produced by the α-decay of ^{238}U, ^{235}U, ^{232}Th and ^{147}Sm in the crystal lattice of zircon and apatite (e.g. Zeitler *et al.* 1987; Lippolt *et al.* 1994; Farley 2002; Reiners *et al.* 2003). The partial retention zone of zircon and apatite is the temperature range in which radiogenic He diffuses out of the zircon (190–120°C) and apatite (80–60°C) crystal (Wolf *et al.* 1996, 1998; Farley 2000; Reiners *et al.* 2003). The effective closure temperatures for ZHe and AHe systems can vary within the ranges of the partial retention zone but are typically reported with 190–150°C for ZHe and 75–50°C for AHe, respectively (Ehlers & Farley 2003; Reiners *et al.* 2004; Reiners & Brandon 2006; Flowers *et al.* 2007; Herman *et al.* 2007; Guenthner *et al.* 2013). The actual closure temperature depends on the He diffusion kinetics of the mineral, which is influenced by factors like its cooling history, the grain size, the experienced radiation damage, as well as the location of the radiation damage within the grain (Flowers *et al.* 2009; Guenthner *et al.* 2013; Danišík *et al.* 2017). Helium diffusivity is higher in zircon that experienced little radiation damage, as *c*-axis parallel diffusion pathways become increasingly blocked. However, with increasing radiation damage this trend is reversed if the amount of radiation reaches a threshold value, where damage zone interconnection causes effective diffusion pathways for radiogenic He (Guenthner *et al.* 2013). The concentration of effective U (eU= (U+0.235)×Th) provides a measure of the radiation damage of a crystal. With the diffusion model of Guenthner *et al.* (2013), moderate eU values determined for our samples, in combination with the young cooling history for samples from footwall units, the thermal modelling with HeFTy implies an effective closure temperature of 170–150°C for the ZHe system. The effect of radiation damage on the He diffusion behaviour in apatite is similar to that of zircon, as He retentively also increases with increasing radiation damage (Flowers *et al.* 2009; Gautheron *et al.* 2009; Shuster & Farley 2009). Given the continuous cooling through the partial retention zone of apatite, and low eU values of 9.5–10.5 ppm, a typical effective closure temperature of samples originating from footwall units is 62°C (Flowers *et al.* 2009). AHe samples from the hanging wall show a wider range of eU

Table 3. *Results of zircon fission-track analyses*

Sample	Number of grains	ρ_s	N_s	ρ_i	N_i	ρ_d	N_d	$P(\chi^2)$ (%)	Dispersion (%)	Central age±1σ (Ma)	U (ppm)
15M45	15	24.508	106	53.408	231	6.458	1982	13.39	5	22.7 ± 2.9	276
15M47	15	20.534	109	32.026	170	6.822	1982	18.91	24	28.2 ± 4.2	152
15M57	20	19.172	147	42.213	316	6.419	1982	19.63	20	19.1 ± 2.4	224
15M59	20	25.519	148	37.071	215	6.404	1982	93.85	1	33.6 ± 4.0	185

ρ_s (ρ_i) is the spontaneous (induced) track density (10^5 tracks per cm^2); N_s (N_i) is the number of counted spontaneous (induced) tracks; ρ_d is the dosimeter track density (10^5 tracks per cm^2); N_d is the number of tracks counted on the dosimeter; $P(\chi^2)$ is the probability of obtaining a Chi-square value (χ^2) for n degree of freedom (where n is the number of crystals minus 1); ages were calculated using the zeta calibration method (Hurford & Green 1983), glass dosimeter IRMM541, and a zeta value of 153 ± 7 a cm^{-2} calculated with Fish Canyon Tuff zircon standards.

values (3.4–234.9 ppm) and inherit a more protracted cooling history. The corresponding effective closure temperature may therefore vary between *c.* 50 and *c.* 75°C, assuming a slow cooling rate of 1°C Ma^{-1} and eU values between 4 and 150 ppm, respectively (Flowers *et al.* 2009).

We employed (U–Th)/He dating on samples containing apatite and zircon of sufficient quality (Table 1). Inclusion- and crack-free apatite and zircon crystals were hand-picked using a stereo- and polarizing microscope and selected under 200× magnification following the selection criteria of Farley (2002) and Reiners (2005). The dimension of the selected crystals was measured to determine alpha-ejection correction factors (Farley *et al.* 1996). Single crystals were loaded into pre-cleaned Pt tubes for He analysis carried out at the GÖochron Laboratory at the University of Göttingen (Germany) and one (U–Th)/He zircon analysis at the University of Tübingen (sample 16M95). At the GÖochron Laboratory at the University of Göttingen, extraction of He from crystals was performed by heating the encapsulated grains in vacuum using an IR laser. The extracted gas was purified by a SAES Ti-Zr getter and the He content was measured by a Hiden Hal-3F/PIC triple-filter quadrupole mass spectrometer. For measurements of the alpha-emitting elements U, Th and Sm, the crystals were dissolved and spiked with calibrated ^{233}U, ^{230}Th and ^{149}Sm solutions. Zircon crystals were dissolved in Teflon bombs with 48% HF and 65% HNO_3 at 220°C for five days. Apatite crystals were dissolved in 2% ultrapure HNO_3 (+0.05% HF) in an ultrasonic bath. The actinide and Sm concentrations were measured by inductively coupled plasma mass spectrometry (ICP-MS) with a Perkin Elmer Elan DRC II system equipped with an APEX micro-flow nebulizer using isotope dilution. Errors for the single-grain ZHe and AHe analyses are attributed to uncertainties in the He, U, Th and Sm measurements and the estimated uncertainty of the Ft correction factor. The zircon and apatite (U–Th)/He ages were calculated as unweighted mean ages from the single-grain ages of each sample and are reported in Tables 4 and 5 with an uncertainty of 1σ standard errors.

Thermokinematic modelling

We used a 1D thermokinematic model to constrain the exhumation history of the Aydın range. The model accounts for vertical heat transport through the Earth's crust by conduction and advection. The code is based on a modified version of *Pecube* (Braun 2003; Braun *et al.* 2012), which solves the advective–conductive heat transfer equation with implicit time stepping and uses a two-step (sampling and appraisal stages of Sambridge (1999*a*) and Sambridge (1999*b*), respectively) neighbourhood algorithm inversion. The heat production in the thermal model is 0.8 µW m^{-3} and the thermal diffusivity is 31.5 km^2 Ma^{-1}. The upper model boundary corresponds to the present-day sample elevation and surface temperature (calculated with a mean annual temperature of 20°C at sea level and an atmospheric lapse rate of 6.5°C km^{-1}). The lower model boundary has a fixed temperature of 750°C, far above the temperature range of the modelled low-temperature thermochronometers. Due to this lower boundary condition, the thickness of the model depends on the geothermal gradient. To prevent an over interpretation of the data and to choose an appropriate dimensionality of the model, we follow the procedure of Glotzbach *et al.* (2011). Each sample is tested for a linear, a two-step, a three-step or a four-step (inversions 1.1, 1.2, 1.3 and 1.4, respectively) exhumation history. The resulting exhumation rates and time periods are reported in Table 6. Adding complexity (such as exhumation steps) to a model generally increases its likelihood to fit the observed data but is also accompanied by an increase in the uncertainty. Relying solely on the loglikelihood function, or another misfit criterion as a selection criterion for the appropriate model setup, would imply a preference for the model with the highest

Table 4. *Results of apatite U–Th/He analyses*

Sample	Aliq.	He		^{238}U			^{232}Th			Th/U ratio	Sm			Sphere equiv. radius (µm)	eU conc. (ppm)	Ejection correction (FT)	Uncorr. age (Ma)	FT-corr. age (Ma)	2σ (Ma)	Sample age (Ma)	1 s.e. (Ma)
		Vol. (10^{-9} cm^3)	1σ (%)	Mass (ng)	1σ (%)	Conc. (ppm)	Mass (ng)	1σ (%)	Conc. (ppm)		Mass (ng)	1σ (%)	Conc. (ppm)								
15M42	#2	0.029	3.6	0.050	2.2	8.4	0.175	2.4	29.1	3.46	1.635	3.5	273	77	15.3	0.80	2.28	**2.85**	0.28		
	#4	0.013	4.9	0.027	6.2	4.3	0.079	2.6	12.7	2.97	1.174	2.2	190	66	7.3	0.77	1.98	**2.57**	0.34	**2.7**	0.1
15M44	#1	0.046	2.8	0.056	2.1	5.5	0.216	2.4	21.1	3.84	3.120	3.1	305	83	10.5	0.82	2.87	**3.51**	0.29	**3.5**	0.3
15M46	#1	0.021	3.7	0.037	4.3	9.3	0.004	19.0	0.9	0.10	0.181	2.2	46	43	9.5	0.65	4.38	**6.73**	1.01	**6.7**	1.0
15M51	#1	0.033	2.9	0.074	2.0	10.8	0.052	2.6	7.6	0.70	0.194	6.8	28	80	12.6	0.81	3.10	**3.82**	0.33		
	#2	0.006	6.9	0.010	7.8	2.9	0.007	4.2	2.3	0.78	0.138	7.1	42	51	3.4	0.71	4.13	**5.85**	1.17	**4.7**	0.6
	#4	0.140	1.8	0.332	1.8	87.5	0.034	2.8	9.0	0.10	0.143	10.4	38	66	89.6	0.77	3.39	**4.38**	0.37		
15M59	#1	0.081	2.2	0.103	1.9	19.2	0.739	2.4	138.0	7.18	0.547	3.8	102	55	51.6	0.73	2.38	**3.27**	0.32		
	#3	2.564	1.2	0.934	1.8	113.2	4.269	2.4	517.5	4.57	0.890	4.2	108	70	234.9	0.78	10.86	**13.84**	1.04		
	#5	1.913	1.4	0.754	1.8	85.5	3.836	2.4	434.8	5.09	0.717	2.2	81	68	187.6	0.78	9.48	**12.18**	0.95	**9.8**	4.6
	#6	0.847	1.4	0.356	1.9	61.6	2.396	2.4	415.1	6.74	0.432	2.2	75	66	159.1	0.77	7.56	**9.79**	0.79		
16M86	#1	0.005	7.2	0.026	6.1	4.3	0.012	3.0	2.0	0.45	0.814	2.2	135	63	4.8	0.76	1.18	**1.55**	0.28		
	#2	0.002	9.3	0.015	11.0	3.5	0.006	11.5	1.4	0.39	0.453	2.2	107	51	3.8	0.70	0.86	**1.22**	0.32	**2.0**	0.7
	#3	0.005	7.1	0.014	10.3	3.1	0.005	10.3	1.2	0.37	0.389	2.2	87	52	3.4	0.71	2.39	**3.37**	0.76		

Ejection correction (Ft): correction factor for alpha-ejection (according to Farley *et al.* (1996)). Uncertainty of the single-grain ages includes both the analytical uncertainty and the estimated uncertainty of the ejection correction. eU is the date-effective uranium concentration ((U + 0.235)×Th). Sample age is the unweighted average age of all Ft-corrected (U-Th)/He ages (se: standard error). Only bold marked single and aliquote ages are used for interpretation.

Table 5. *Results of zircon U–Th/He analyses*

		He		^{238}U			^{232}Th				Sm										
Sample	Aliq.	Vol. (10^{-9} cm^3)	1σ (%)	Mass (ng)	1σ (%)	Conc. (ppm)	Mass (ng)	1σ (%)	Conc. (ppm)	Th/U ratio	Mass (ng)	1σ (%)	Conc. (ppm)	eU Conc. (ppm)	Sphere equiv. radius (μm)	Ejection correct. (FT)	Uncorr. age (Ma)	FT-corr. age (Ma)	2σ (Ma)	Sample age (Ma)	1 s.e. (Ma)
15M44	#1	3.860	1.3	2.466	1.8	165.9	0.381	2.4	25.7	0.15	0.215	15.7	1	171.9	74	0.81	12.50	**15.3**	1.08		
15M44	#3	4.250	1.3	3.150	1.8	497.2	0.821	2.4	129.6	0.26	0.453	15.7	7	527.6	67	0.80	10.51	**13.2**	0.98	**14.3**	1.5
15M46	#1	8.094	1.3	4.291	1.8	1063.9	1.200	2.4	297.4	0.28	0.272	15.7	7	1133.8	51	0.74	14.64	**19.9**	1.78		
15M46	#2	0.923	1.4	0.634	1.8	264.6	0.307	2.4	128.0	0.48	0.336	15.7	14	294.6	55	0.76	10.77	**14.2**	1.21		
15M46	#3	1.287	1.4	1.008	1.8	533.0	0.202	2.4	106.9	0.20	0.155	15.7	8	558.1	48	0.70	10.08	**14.3**	1.42	**16.2**	1.9
15M47	#1	0.806	2.6	3.739	1.8	1165.3	0.609	2.4	189.9	0.16	0.368	15.7	11	1209.9	48	0.72	1.72	**2.4**	0.25		
15M47	#2	1.724	1.4	1.016	1.8	222.3	0.729	2.4	159.5	0.72	0.562	15.7	12	259.8	62	0.78	11.96	**15.3**	1.18	**15.31**	1.18
15M55	#2	1.217	1.4	0.907	1.8	159.1	0.286	2.4	50.1	0.32	0.407	15.7	7	170.9	56	0.76	10.30	**13.6**	1.14	**13.56**	1.14
15M56	#1	3.833	1.3	1.611	1.8	439.0	0.097	2.5	26.5	0.06	0.179	15.7	5	445.2	58	0.77	19.39	25.3	2.10		
15M56	#2	0.804	1.5	0.491	1.9	278.7	0.084	2.5	47.9	0.17	0.220	15.7	12	289.9	45	0.70	12.98	**18.5**	1.86	**16.8**	2.4
15M56	#3	0.375	1.5	0.264	2.0	351.4	0.127	2.4	168.1	0.48	0.116	15.7	15	390.9	44	0.69	10.51	**15.2**	1.56		
15M56	#4	1.652	1.4	0.611	1.8	457.5	0.411	2.4	308.0	0.67	0.063	15.7	5	529.9	45	0.70	19.27	27.5	2.71	26.4	1.5
15M57	#1	4.611	1.3	3.151	1.8	590.5	0.502	2.4	94.2	0.16	0.302	15.7	6	612.6	61	0.78	11.67	**15.0**	1.18		
15M57	#2	5.701	1.3	3.664	1.8	831.9	0.273	2.4	62.1	0.07	0.210	15.7	5	846.5	231	0.94	12.66	**13.5**	0.63		
15M57	#3	6.538	1.3	4.883	1.8	1291.1	0.528	2.4	139.6	0.11	0.406	15.7	11	1323.9	57	0.76	10.81	**14.1**	1.17	**14.2**	0.4
15M58	#1	4.466	1.3	3.068	1.8	92.7	1.271	2.4	38.4	0.41	0.994	15.7	3	101.7	96	0.86	10.95	**12.8**	0.76		
15M58	#2	11.496	1.3	8.473	1.8	476.2	1.118	2.4	62.9	0.13	0.408	15.7	2	491.0	88	0.84	10.89	**12.9**	0.82		
15M58	#3	9.012	1.3	5.666	1.8	351.4	2.050	2.4	127.1	0.36	0.740	15.7	5	381.2	92	0.85	12.12	**14.3**	0.87	**13.3**	0.5
15M59	#1	1.085	2.3	3.221	1.8	604.4	0.270	2.4	50.6	0.08	0.335	15.7	6	616.3	79	0.83	2.74	**3.3**	0.26		
15M59	#2	1.598	1.4	0.692	1.8	57.3	0.333	2.4	27.6	0.48	0.327	15.7	3	63.8	77	0.82	17.09	**20.8**	1.42		
15M59	#3	3.984	1.3	1.734	1.8	192.0	0.316	2.4	35.0	0.18	0.768	15.7	9	200.2	75	0.82	18.17	**22.2**	1.53	**21.5**	1.0
16M87	#1	4.81	1.1	2.33	1.8	167	1.94	2.4	139	0.83	0.050	11.9	4	199.8	87	0.84	14.3	**17.0**	1.0		
16M87	#2	3.62	1.1	2.37	1.8	432	0.56	2.4	103	0.24	0.024	8.6	4	456.5	54	0.75	12.0	**15.9**	1.3		
16M87	#3	2.45	1.1	1.13	1.8	672	0.37	2.4	220	0.33	0.014	11.1	8	723.7	45	0.70	16.7	**23.9**	2.4	**18.9**	2.5
16M89	#1	3.69	1.0	2.34	1.8	504	0.12	2.4	25	0.05	0.012	5.0	3	510.4	68	0.80	12.9	**16.1**	1.2		
16M89	#3	5.71	1.1	3.25	1.8	754	0.68	2.4	158	0.21	0.028	3.3	7	791.4	68	0.80	13.9	**17.4**	1.3	**16.8**	0.9
16M90	#2	4.47	1.1	2.49	1.8	462	1.60	2.4	297	0.64	0.027	9.5	5	532.1	54	0.75	12.9	**17.3**	1.5		
16M90	#3	3.64	1.0	2.04	1.8	406	0.13	2.4	25	0.06	0.009	15.8	2	411.7	46	0.71	14.5	**20.4**	2.0	**18.9**	2.2
16M91	#1	1.65	1.1	1.06	1.8	104	0.51	2.4	50	0.48	0.041	5.9	4	115.4	69	0.80	11.6	**14.5**	1.0		
16M91	#2	1.00	1.2	0.43	1.9	129	0.51	2.4	152	1.18	0.011	6.7	3	164.3	53	0.75	15.1	**20.2**	1.7		
16M91	#3	6.74	1.0	3.15	1.8	121	2.70	2.4	103	0.86	0.064	8.9	2	145.0	118	0.88	14.7	**16.7**	0.8	**17.1**	1.7
16M95*	#1	0.99	1.2	0.61	3.5	-	0.39	3.8	-	0.63	-	-	-	433.3	35	0.62	11.5	**18.5**	0.4		
16M95*	#2	2.30	1.2	1.25	5.0	-	0.46	4.8	-	0.37	-	-	-	206.6	298	0.95	14.0	**14.7**	0.7		
16M95*	#3	0.23	1.3	0.14	7.4	-	0.11	5.6	-	0.75	-	-	-	206.2	36	0.63	11.6	**18.4**	0.7	**17.2**	1.2

Ejection correction (Ft): correction factor for alpha-ejection (according to Farley *et al.* (1996) and Hourigan *et al.* (2005)). Uncertainty of the single-grain ages includes both the analytical uncertainty and the estimated uncertainty of the ejection correction. Sample age is the unweighted average age of all Ft-corrected (U–Th)/He ages. eU is the date-effective uranium concentration ((U + 0.235)×Th). Results from aliquots marked with an asterisk were measured in the laboratory in Tübingen. Single and aliquot ages marked in grey indicate hanging-wall population in sample 15M56.

Table 6. *Parameters for inversions 1.1 to 1.4 and resulting exhumation rates (E) for different time periods (T)*

			Inversion results							
			1.1		1.2		1.3		1.4	
Parameter	Unit	Range	Mean	s.e.	Mean	s.e.	Mean	s.e.	Mean	s.e.
Sample 14M31 (ZFT, ZHe, AFT, AHe)										
E_1 (0 Ma–T_1)	(km Ma^{-1})	0–1.5	0.52	0.10	0.94	0.29	0.98	0.21	1.04	0.26
T_1	(Ma)	0–35			2.18	1.37	2.95	0.65	1.96	1.12
E_2 (T_1–T_2)	(km Ma^{-1})	0–1.5			0.13	0.03	0.30	0.35	0.11	0.12
T_2	(Ma)	0–35					6.65	8.50	15.29	11.40
E_3 (T_2–T_3)	(km Ma^{-1})	0–1.5					0.56	0.45	0.43	0.38
T_3	(Ma)	0–35							21.30	8.95
E_4 (T_3–T_{max})	(km Ma^{-1})	0–1.5							0.63	0.38
Geothermal gradient	(C° km^{-1})	30–50	38.84	5.76	39.61	5.51	37.76	5.78	36.72	4.41
Number of iterations			50		150		400		450	
Number of parameters			2		4		6		8	
Number of observations			7		7		7		7	
Log-likelihood			−175.45		−13.69		−8.40		−7.73	
BIC			354.80		35.17		**28.48**		31.04	
Sample 14M37 (ZFT, ZHe, AFT, AHe)										
E_1 (0 Ma–T_1)	(km Ma^{-1})	0–1.5	0.20	0.04	0.14	0.09	0.12	0.10	0.11	0.08
T_1	(Ma)	0–26			14.29	6.32	13.81	5.32	14.06	5.45
E_2 (T_1–T_2)	(km Ma^{-1})	0–1.5			0.47	0.32	0.63	0.39	0.55	0.39
T_2	(Ma)	0–26					14.16	5.88	15.05	6.02
E_3 (T_2–T_3)	(km Ma^{-1})	0–1.5					0.49	0.33	0.65	0.42
T_3	(Ma)	0–26							16.28	4.04
E_4 (T_3–T_{max})	(km Ma^{-1})	0–1.5							0.48	0.36
Geothermal gradient	(C° km^{-1})	30–50	39.32	5.75	38.40	5.36	38.76	5.31	36.91	5.35
Number of iterations			50		150		300		350	
Number of parameters			2		4		6		8	
Number of observations			6		6		6		6	
Log-likelihood			−17.20		−2.73		−1.38		−2.37	
BIC			37.18		**12.63**		13.50		19.08	
Sample 15M44 (ZFT, ZHe, AFT, AHe)										
E_1 (0 Ma–T_1)	(km Ma^{-1})	0–1.5	0.27	0.05	0.53	0.26	0.42	0.17	0.42	0.19
T_1	(Ma)	0–26			7.74	7.24	7.29	6.36	12.74	8.91
E_2 (T_1–T_2)	(km Ma^{-1})	0–1.5			0.24	0.26	0.29	0.29	0.19	0.22
T_2	(Ma)	0–26					9.62	8.05	12.72	8.30
E_3 (T_2–T_3)	(km Ma^{-1})	0–1.5					0.37	0.37	0.44	0.42
T_3	(Ma)	0–26							13.98	5.97
E_4 (T_3–T_{max})	(km Ma^{-1})	0–1.5							0.41	0.36
Geothermal gradient	(C° km^{-1})	30–50	39.12	5.86	37.62	5.32	37.49	5.00	36.33	5.60
Number of iterations			50		150		300		350	
Number of parameters			2		4		6		8	

(continued)

Table 6. (Continued)

			Inversion results							
			1.1		1.2		1.3		1.4	
Parameter	Unit	Range	Mean	s.e.	Mean	s.e.	Mean	s.e.	Mean	s.e.
Number of observations			5		5		5		5	
Log-likelihood			−24.15		−14.72		−11.88		−12.79	
BIC			50.49		35.88		**33.42**		38.45	
Sample 15M57/16M97 (ZFT, ZHe, AFT)										
E_1 (0 Ma–T_1)	(km Ma^{-1})	0–1.5	0.25	0.05	0.18	0.10	0.18	0.14	0.18	0.13
T_1	(Ma)	0–25			13.45	4.93	12.18	4.99	12.41	4.45
E_2 (T_1–T_2)	(km Ma^{-1})	0–1.5			0.79	0.39	0.68	0.41	0.58	0.36
T_2	(Ma)	0–25					14.30	4.53	14.43	4.94
E_3 (T_2–T_3)	(km Ma^{-1})	0–1.5					0.81	0.37	0.73	0.41
T_3	(Ma)	0–25							16.05	3.88
E_4 (T_3–T_{max})	(km Ma^{-1})	0–1.5							0.78	0.40
Geothermal gradient	(C° km^{-1})	30–50	39.46	5.78	38.93	5.77	38.39	5.90	38.35	5.40
Number of iterations			50		150		300		350	
Number of parameters			2		4		6		8	
Number of observations			5		5		5		5	
Log-likelihood			−15.19		−3.83		−0.93		−3.51	
BIC			33.61		14.10		**10.17**		19.90	

BIC, Bayesian information criterion.Parameters T_1 and T_2 denote the time (from 0 Ma to T_{max}) at which exhumation rates change. Parameters E_1, E_2, E_3 and E_4 are the exhumation rates (from 0 to 1.5 km Ma^{-1}) between 0 Ma and T_1 (E_1), between T_1 and T_2 (E_2), between T_2 and T_3 (E_3) and T_3 and T_{max} (E_4). Entries in grey indicate parameters that resulted in the arithmetic mean of their boundary limits and are not used for interpretation.

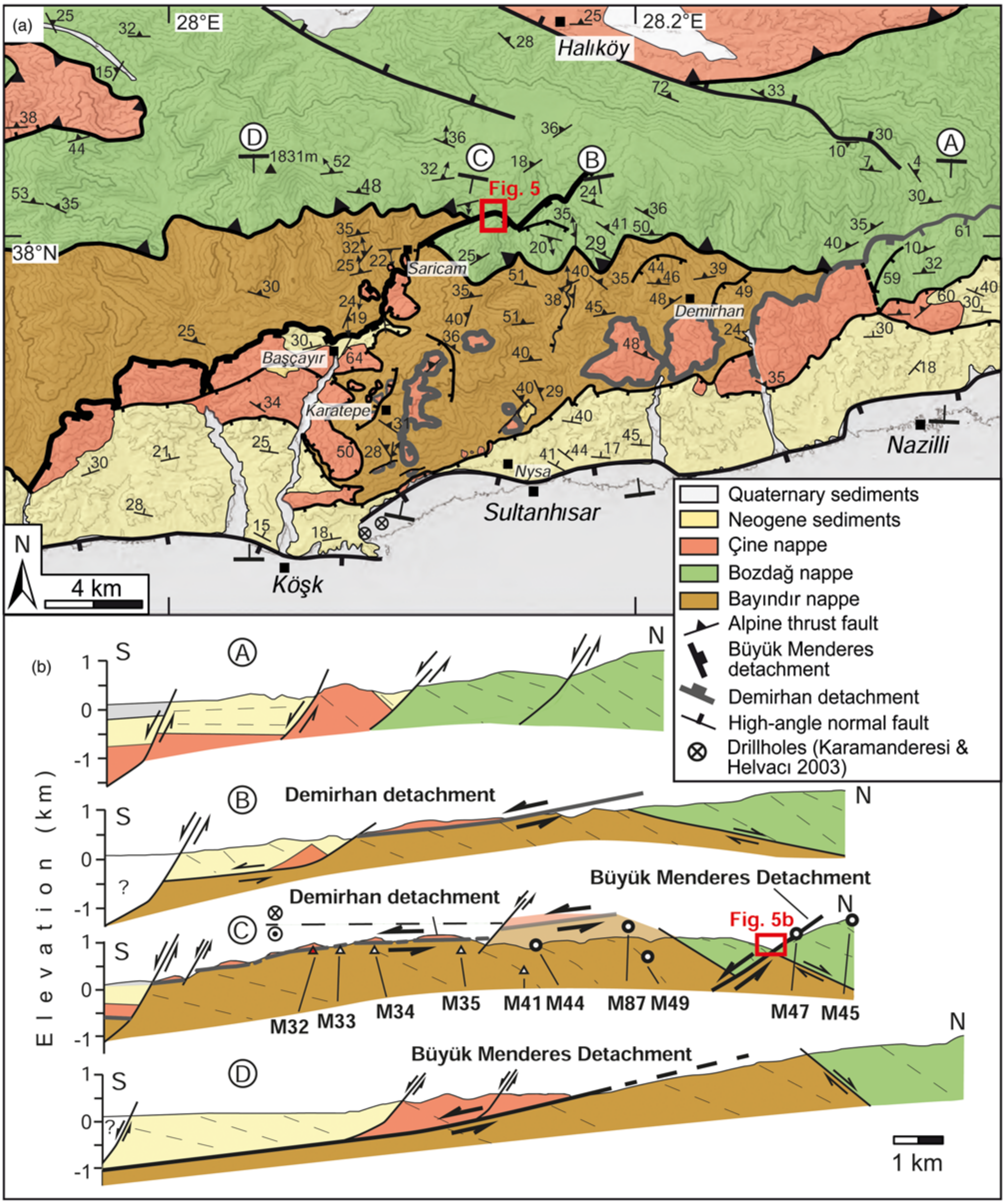

Fig. 3. (**a**) Geological map of the eastern part of the Aydın range between Köşk and Nazilli. (**b**) Geological cross-sections along the southern flank of the Aydın range. Map and profiles are based on our own observations and data from previous studies (Karamanderesi & Helvacı 2003; Rojay *et al.* 2005; Çemen *et al.* 2006; Emre & Sözbilir 2007; Sen & Seyitoğlu 2009; Candan *et al.* 2011; Yal *et al.* 2017).

complexity. Therefore, we employ the Bayesian information criterion (BIC), which provides a measure of the ratio between the likelihood (fitting) and the model complexity (Schwarz 1978):

$$BIC = -2 \cdot \ln L + k \cdot \ln(n) \quad (1)$$

whereby ln$L$ denotes the log-likelihood for the model, and k and n are the numbers of free parameters and observations, respectively. Thus, the lowest BIC value indicates the preferred model setup. Depending on the number of time/exhumation steps, we model 5000 to 35 000 thermal histories, over the last 26 Ma for footwall samples from the Demirhan and Büyük Menderes detachment, and 5000 to 45 000 thermal histories over the last 35 Ma for samples from the hanging wall. Free parameters are the geothermal gradient (30–50°C km^{-1}), the exhumation rates (0–1.5 km Ma^{-1}) and the time at which the exhumation rate changes (in the period between 0–26 and 0–35 Ma for the footwall and hanging wall, respectively). The thermokinematic model traces the cooling history of rocks based on the modelled exhumation paths and calculates thermochronological ages with the annealing algorithms of Ketcham *et al.* (2007) and Tagami *et al.* (1998) for AFT and ZFT, and the diffusion algorithms of Flowers *et al.* (2009) and Guenthner *et al.* (2013) for AHe and ZHe. The probability of each free input parameter is derived from the appraisal stage of the neighbourhood inversion (Sambridge 1999*b*) and is visualized as 1D and 2D marginal probability density functions (PDFs). Probable exhumation paths are visualized as synoptic 2D marginal PDFs, in which re-sampled exhumation rates and the time at which exhumation rates changed were linked to visualize the exhumation rate changing with time. For details on the modelling approach the reader is referred to Glotzbach *et al.* (2011) and recent studies of Schultz *et al.* (2017), Thiede & Ehlers (2013) and Whipp *et al.* (2007), which also used the advances of comparable 1D thermokinematic modelling approaches to infer exhumation rates from low-temperature thermochronology data.

Results

Geological mapping of extensional structures

Mapping in the Aydın range aimed at (a) identifying the tectonic structures that document the Cenozoic extensional history of the southern part of the central Menderes Massif and (b) linking these structures to the low-temperature thermochronological data. The field relations revealed that two detachment faults are exposed along the southern flank of the Aydın range, which we call the Büyük Menderes and Demirhan detachments, respectively. We focused our thermochronological and structural studies on two areas where the Büyük Menderes and Demirhan detachments are particularly well exposed; the region between Başçayır and Nazilli (Fig. 3) and the area around Beyköy (Fig. 4).

The western part of the south-dipping Büyük Menderes detachment fault strikes WSW–ENE and can be traced from Beyköy in the west (Fig. 2b) to the central part of the Aydın range, *c.* 9 km south of Halıköy (Fig. 2a). The footwall of the detachment dips with 14–20° to the south or SSE and shows consistent south- to SSW-dipping slickenline lineations on the detachment surface. The cataclasites overprint a mylonitic footwall with top-to-the-south shear sense indicators (Fig. 2f). Apart from the eastern termination of the Büyük Menderes detachment, where the footwall consists of garnet-bearing mica schists of the Bozdağ nappe, footwall rocks of the Büyük Menderes detachment exclusively consist of phyllites, marble lenses and mica schists of the Bayındır nappe. The hanging wall is comprised of augengneisses and partly paragneisses of the Çine nappe which are overlain by northward-dipping Neogene sediments. Gürer *et al.* (2009) previously reported that the trace of the Büyük Menderes detachment east of Başçayır village is displaced by an approximately north–south-striking fault, which explained the reappearance of the detachment SE of Başçayır village at Karatepe (Fig. 3a). Instead, our own mapping in the area around Başçayır

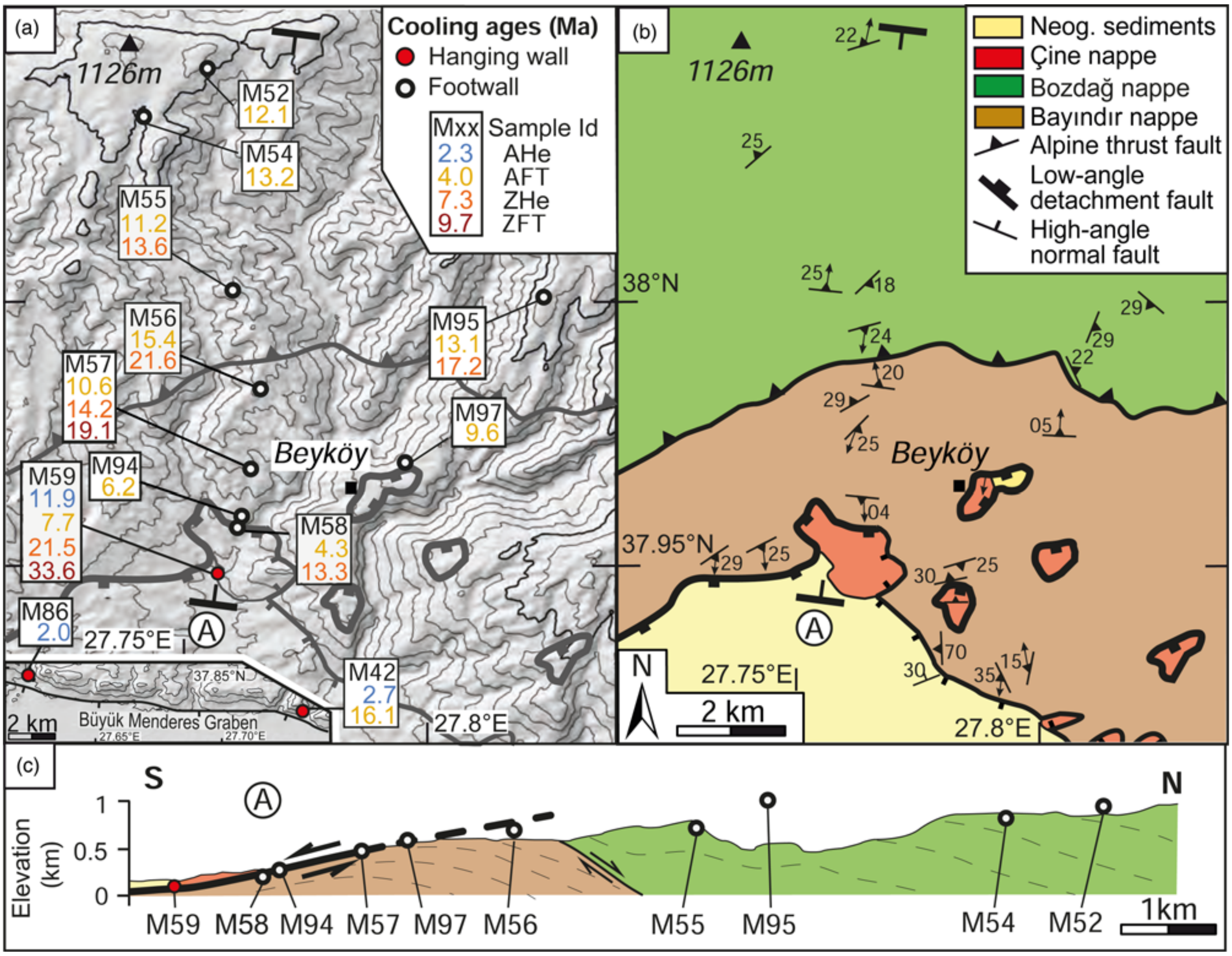

Fig. 4. (**a**) Shaded relief image of the western part of the Aydın range with thermochronological sample locations and the associated cooling ages. Note that for clarity the first two digits of the thermochronological sample identifiers are omitted. Inset shows the position of AHe samples from the northern rim of the Büyük Menderes graben. (**b**) Geological map of the same area showing relicts of Çine nappe klippen at Beyköy resting on phyllites of the Bayındır nappe. (**c**) Position of the low-temperature thermochronology samples projected orthogonally into the NNE–SSW-trending geological cross-section.

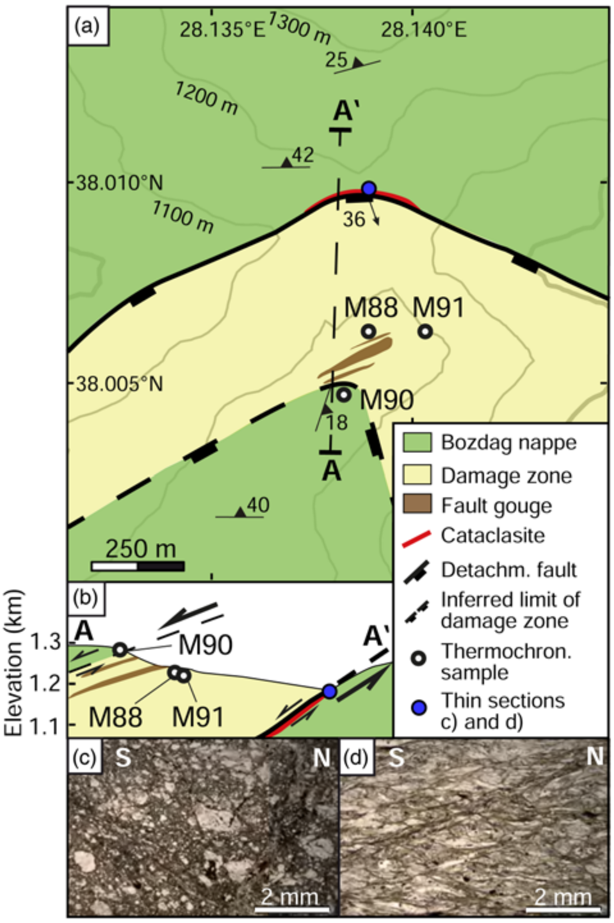

Fig. 5. (**a**) Detailed geological map of the eastern part of the Büyük Menderes detachment, NE of Sariçam village. (**b**) Cross-section of the fault zone which is characterized by a wide damage zone above a cataclasite and *c.* 3 m thick fault gouge horizons. Open circles indicate the position of the thermochronology samples. (**c**) Thin section of the cataclastic footwall showing cataclastically reworked components. (**d**) Thin section of a footwall sample taken 2 m below the cataclasite revealing mylonitic textures with C/S fabrics indicating dextral (top-south) shearing.

village revealed that the Büyük Menderes detachment can be traced further to the NE of Sariçam village (Fig. 3a). Here, the Büyük Menderes detachment occurs as a 1–2 m thick south-dipping (185°/36°) cataclasite with slickenlines dipping 168°/22° (Fig. 5a and b). Thin sections document the cataclastic overprint of a ductilely deformed footwall (Fig. 5c). Ductile top-to-the-south shearing is documented by S–C fabrics and mica fish in thin section (Fig. 5d). A *c.* 300 m thick damage zone above the cataclasite contains 3–6 m thick fault gouge horizons that seem to represent the upper limit of the damage zone (Fig. 5b). In contrast to other parts of the Büyük Menderes detachment, both hanging wall and footwall consist of garnet mica schist of the Bozdağ nappe, which implies that the outcrop represents a structurally higher part of the detachment fault. The eastern termination of the Büyük Menderes detachment, *c.* 9 km south of Halıköy (Fig. 3a), is characterized by scarce cataclasite relicts and fractured mica schists with thin fault gouge horizons.

The Demirhan detachment

The NE-trending trace of the southward-dipping Büyük Menderes detachment in the Başçayır area (Fig. 2a), and the tectonic contact between the Bayındır nappe and the Çine nappe exposed farther south and east of Karatepe (Fig. 2c–e), indicate that they cannot be part of the same detachment fault (Fig. 3, cross-section C). Instead, we propose that this fault contact represents a separate, eastern branch of the Büyük Menderes detachment system, which we have called the Demirhan detachment. The Demirhan detachment is structurally located in the hanging wall of the Büyük Menderes detachment and can be traced as a WSW–ENE-striking fault, from the mountains north of Sultanhisar over *c.* 20 km to the mountains north of Nazilli (Figs 2c and 3). The dip of the Demirhan detachment changes along strike, from a subhorizontal orientation at Karatepe to a 13–16° dip near Demirhan village. Here, the fault contact between phyllites in the footwall and orthogneisses in the hanging wall is well exposed by a cataclastic footwall and *c.* 5 m thick fault gouge horizons (Fig. 2e). A progressive change to high-angle normal faults, which dip with *c.* 60° to the south, occurs in the area north of Nazilli, implying a decreasing fault offset towards the east (Fig. 3b, section A). At Karatepe, a SSW–NNE-striking and NW-dipping normal fault, which can be traced from Sarıçam to Karatepe, cuts and displaces the Demirhan detachment. This fault is exposed along the western slope of the Karatepe ridge, between the Çine and Bayındır nappes. South of Sarıcam, this normal fault dips with 42° to the WNW (Fig. 2h). East of Başçayır, the same normal fault has an orientation of (299°/30°) and the marble-bearing footwall shows slickenlines plunging towards the WNW (298°/30°) (Fig. 2g), indicating a top-to-the-WNW displacement. Therefore, the western termination of the Demirhan detachment is not exposed.

Along the southern part of the Aydın range, east–west-striking high-angle normal faults crosscut and displace the Demirhan detachment towards the uplifted Neogene sediments, which are located north of the active graben-bounding normal fault of the Büyük Menderes graben. In the vicinity of the ancient city of Nysa (Fig. 3a), the eastern branch of the Büyük Menderes detachment crops out as a 3–5 m thick fault gouge zone between phyllites in the footwall and strongly fractured orthogneiss covered by Neogene sediments in the hanging wall (Fig. 2i and j). The southward continuation of the detachment was also encountered in two boreholes in the northern Büyük Menderes graben located *c.* 5 km NE of Köşk (Karamanderesi & Helvacı 2003). In the boreholes, the fault zone is located at a depth of *c.* 500 m and separates orthogneisses from phyllites.

Results from fission-track and (U–Th)/He analysis

Our new low-temperature thermochronology data reveal three distinct age groups, which can be attributed to the cooling and exhumation of the footwall and hanging-wall units of the Büyük Menderes and Demirhan detachments (Figs 6 and 7).

Two AHe ages from the footwalls of both detachments are 3.5 ± 0.3 Ma (sample 15M44) and 6.7 ± 1.0 Ma (sample 14M46). The AFT ages of footwall samples from the Büyük Menderes detachment range from 15.4 ± 2.4 (15M56) to 4.3 ± 0.7 Ma (15M58) and samples from below the Demirhan detachment yielded ages of 12.9 ± 1.3 to 6.0 ± 1.0 Ma (Table 2). The AFT track lengths of 13.0 ± 0.9 to 13.8 ± 1.2 µm for footwall samples of the Büyük Menderes detachment require moderate to fast cooling through the partial annealing zone of the AFT system (Wölfler *et al.* 2017). The majority of AFT samples have similar annealing kinetics, as shown by Dpar values (the arithmetic mean fission-track etch figure parallel to the crystallographic *c*-axis) of 1.2 to 2.2 µm, indicative of F-apatite (Carlson *et al.* 1999). The two AFT samples with Dpar values close to 3 µm (14M42 and 14M45) might be more resistant to annealing (Ketcham *et al.* 1999). ZHe analysis from footwall samples yielded ages between 18.9 ± 2.2 Ma (sample 16M90) and 13.3 ± 0.5 Ma (sample 15M58) (Fig. 6 and Table 5). These ages are mean ages calculated from single grain ages (neglecting one outlier in 15M47). Two age groups were identified within the single-grain analyses of sample 15M56 (Table 5), whereas single grain ages reveal a positive age–eU relationship,

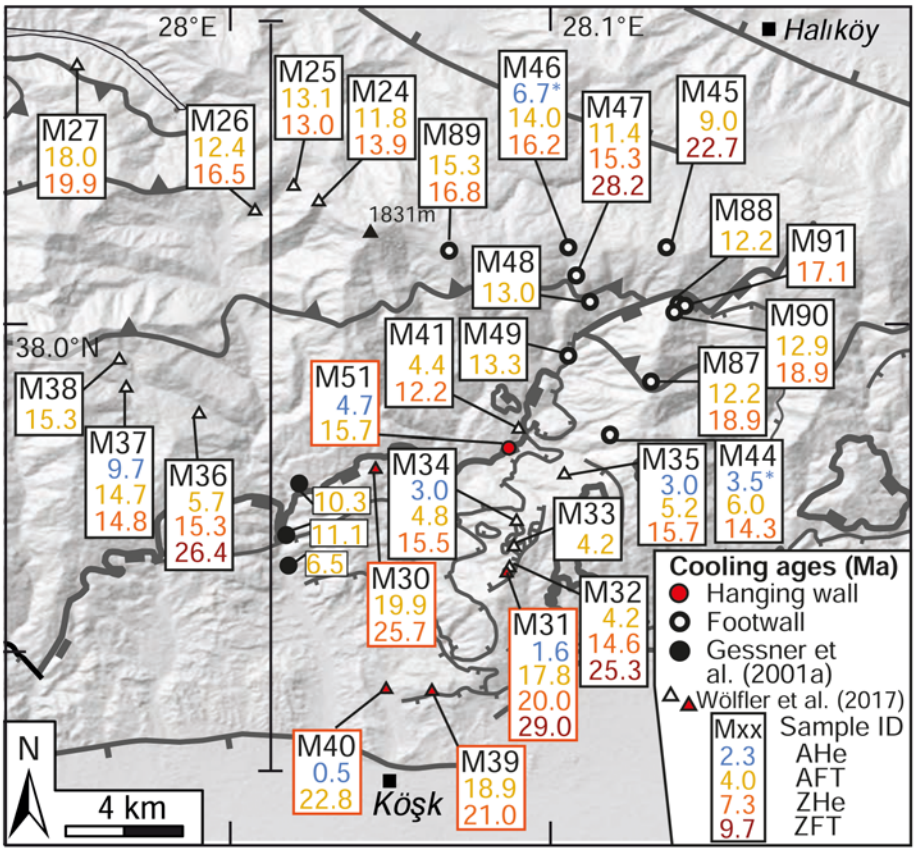

Fig. 6. Shaded relief image of the Aydın range north of Köşk showing thermochronological sampling sites and results of new data presented in this study and data of Wölfler *et al.* (2017) and Gessner *et al.* (2001*a*).

with an eU value of 390.9 ppm for the youngest grain (15.2 ± 1.6 Ma) and an eU value of 529.9 ppm for the oldest grain (27.5 ± 2.7 Ma), which might explain the observed dispersion. However, thermal history modelling taking into account differences in diffusion kinetics caused by grain size and accumulated radiation damage revealed that the grains of the aliquot cannot have experienced the same cooling path. Hence, the two mean ages of 26.4 ± 1.1 Ma and 16.8 ± 1.7 Ma might rather reflect hanging-wall and footwall cooling ages, respectively, as 15M56 shows a strong cataclastic overprint and may include slices of hanging-wall material (Fig. 7b). The youngest and oldest ZFT ages obtained from footwall units are 19.1 ± 2.4 Ma and 28.2 ± 4.2 Ma, respectively (Fig. 7 and Table 3).

AHe ages obtained from samples in the hanging wall of the Büyük Menderes detachment comprise ages ranging from 11.9 ± 1.2 to 2.0 ± 0.7 Ma. The youngest AHe ages of 2.0 Ma (16M86) and 2.7 Ma (15M42) stem from samples near the active normal fault of the Büyük Menderes graben (Fig. 4a). Sample 15M59 from the hanging wall of the Büyük Menderes detachment experienced a slow cooling history, as seen from a late Oligocene ZFT age of 33.6 ± 4.0 Ma, an early Miocene ZHe age (21.5 ± 1.0 Ma) and a late Miocene AFT age of 7.9 ± 1.3 Ma. Four AHe analyses of this sample gave a large range of single grain ages of 13.8 to 3.3 Ma (Table 4). The single grain ages show a positive age–eU relationship, suggesting slow cooling through the partial retention zone. Thermal modelling with HeFty (Ketcham 2005) implies slow cooling since *c.* 20 Ma and an effective closure temperature of *c.* 68°C for the high eU apatite (grains #3, #5, #6) and 60°C for the low eU apatite (grain #1), with a young AHe age of 3.3 Ma.

Data interpretation and discussion

Cooling history of the Aydın range

To analyse the cooling and exhumation history of the rocks in the Aydın range, we complement our new thermochronological data with the data published by Wölfler *et al.* (2017). The combined dataset shows that rocks of the Aydın range can be classified into three groups with different cooling histories. Two groups are attributed to contrasting cooling histories in the footwalls of the Büyük Menderes and the Demirhan detachments, respectively, whereas the third data group documents the cooling of the hanging-wall units above both detachments. Samples from the eastern (Fig. 7a) and western thermochronological transects (Fig. 7b) of the footwall of the Büyük Menderes detachment (Fig. 4a) have in common that both share a rapid cooling event between ZHe and AFT closure temperatures during the middle Miocene. In the eastern part of the footwall of the Büyük Menderes detachment, late Oligocene to early Miocene ZFT ages suggest moderate cooling rates in the early Miocene between ZFT and ZHe systems and an interval of increased rates in the middle Miocene between ZHe and AFT systems – i.e. in a temperature range from *c.* 160–*c.* 110°C (Fig. 7a). In contrast, sample 15M57 in the footwall of the western part of the Büyük Menderes detachment reveals a more progressive cooling from *c.* 19–*c.* 10 Ma between ZFT and AFT systems. This suggests that the detachment operated at higher temperatures, which is supported by intense ductile top-to-the south shearing in the footwall near Beyköy (Fig. 2f). The middle Miocene episode of fast cooling along the footwall of the Büyük Menderes detachment is not observed in thermochronological data from the footwall of the Demirhan detachment (14M32 to 14M35 and 15M44, 16M87, 16M90). Instead, an episode of rapid cooling is recorded between AFT ages ranging between *c.* 6 and *c.* 4 Ma and AHe ages ranging between *c.* 3.5 and *c.* 3.0 Ma in the latest Miocene and Pliocene. Two footwall samples in the Aydın range (16M87 and 16M90) neither show the middle Miocene nor the latest Miocene/Pliocene episodes of enhanced cooling (Fig. 6). The slow and continuous Miocene cooling of these samples can be explained by their structural position in the hanging wall of the Büyük Menderes detachment and the large distance to the Demirhan detachment (Fig. 6). The third group of thermochronological

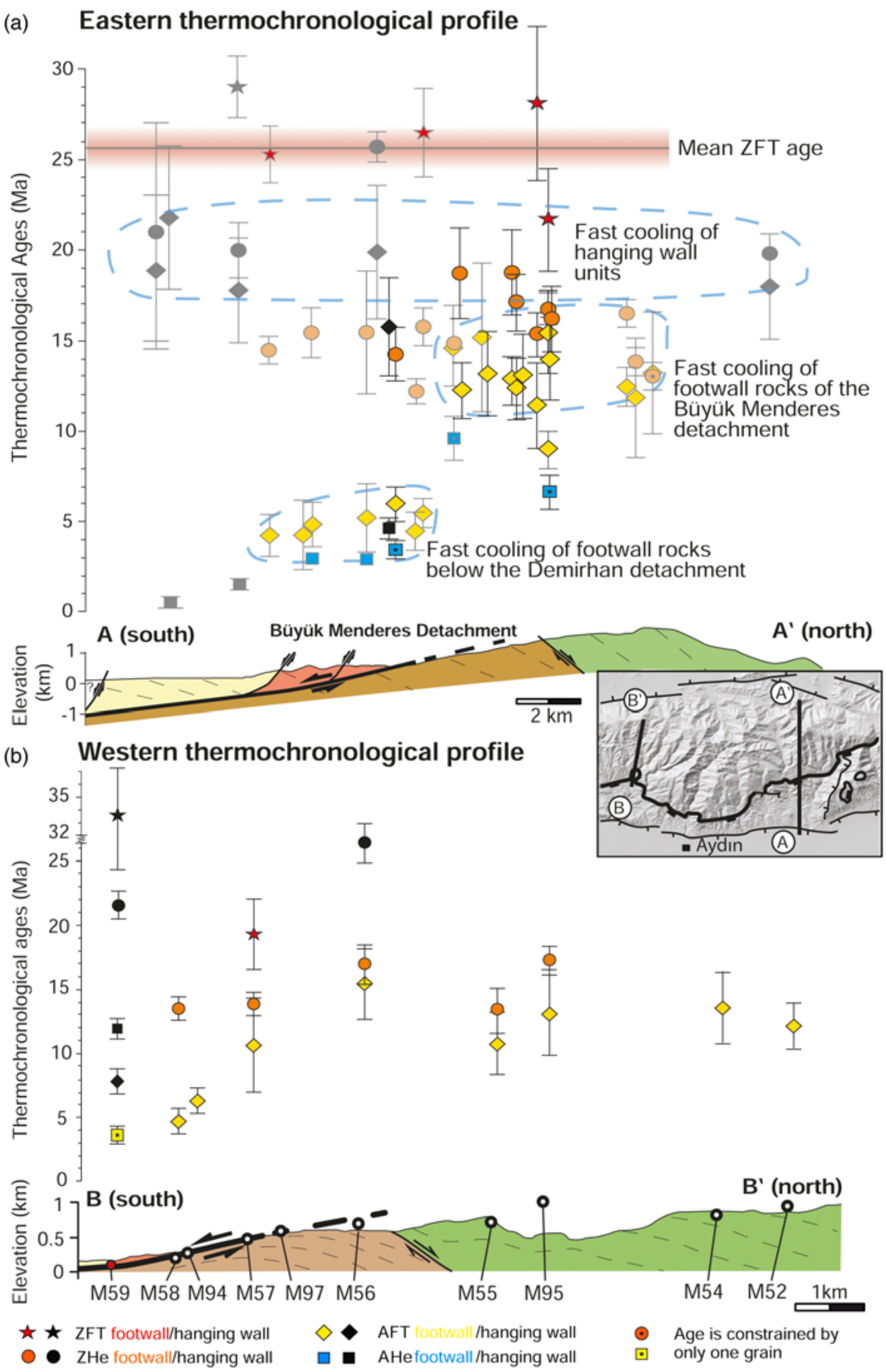

Fig. 7. (**a**) Thermochronological results projected perpendicularly into the extended north–south profile D shown in Figure 3b and depicted in the map inset. (**b**) Thermochronological results of the western thermochronological profile. The ages are projected perpendicular to the NNE–SSW-trending cross-section of Figure 4c. Note that the cooling age axis is not continuous between 26.5 and 32 Ma.

data represents the augengneisses of the Çine nappe that are found as klippen in the hanging walls of the Büyük Menderes and Demirhan detachments. The distinctly older cooling ages of these klippen reveal a phase of relatively rapid cooling in the late Oligocene/early Miocene, which is also described in the Bozdağ range and in the northern Menderes sub-massifs (Gessner *et al.* 2001*b*; Thomson & Ring 2006; Buscher *et al.* 2013; Wölfler *et al.* 2017). However, only in the northern sub-massif can this cooling episode be clearly linked to tectonic denudation along the Simav detachment (Ring *et al.* 2003; Thomson & Ring 2006; Cenki-Tok *et al.* 2016). The AHe ages derived from hanging-wall samples, which are situated in the vicinity of the Büyük Menderes graben, consistently reveal enhanced late Pliocene/Quaternary cooling (Figs 4a and 6) that we interpret to be related to the exhumation in the footwall of the northern graben-bounding normal fault.

Thermokinematic modelling results

To obtain precise predictions on the magnitude and temporal changes in the exhumation history, thermokinematic modelling was performed on samples for which ages from at least three out of the four thermochronometers (AHe, AFT, ZHe, ZFT) were available. Using less thermochronometers usually results in models with limited quantitative information, which was also reported in similar thermokinematic modelling approaches by Valla *et al.* (2010) and van der Beek *et al.* (2010). Two samples from the footwall of the Büyük Menderes detachment (14M37, 15M57), one sample from the footwall of the Demirhan detachment (15M44) and one sample from the hanging wall of the Demirhan detachment (14M31) passed these criteria. The modelled ages of these samples reproduce well the observed thermochronological ages and were used to constrain the exhumation history of the Aydın range (Fig. 8). As samples

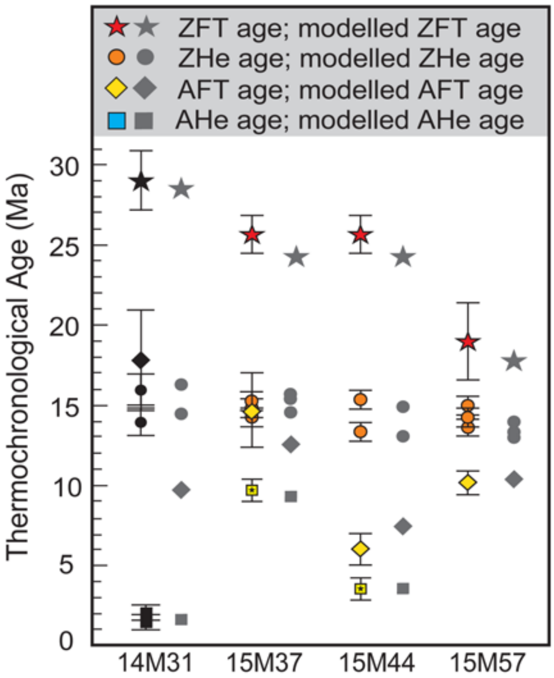

Fig. 8. Observed v. modelled cooling ages, using the same symbols for the thermochronological systems as in Figure 7.

14M37 and 15M44 do not comprise ZFT ages, we used the mean of all available ZFT ages from footwall units in the Aydın range (25.7 ± 1.1 Ma) for the modelling of samples 14M37 and 15M44. The procedure is justified by similar ZFT ages in the footwall and hanging wall of the Aydın range (29–23 Ma), supporting the interpretation of Wölfler *et al.* (2017) that detachment faulting in the eastern part of the Aydın range mainly occurred at or below *c.* 250°C.

The activity of the Büyük Menderes detachment is constrained by samples 15M57 and 14M37 from the western and eastern parts of its footwall. The exhumation history of sample 14M37 is best described by two time-steps (inversion 1.2, Table 6) with a lower BIC value compared to a three-step model or a continuous exhumation model. The model reflects an exhumation history where an early to middle Miocene period with exhumation rates of 0.5 km Ma^{-1} is followed by slower rates of *c.* 0.1 km Ma^{-1} since *c.* 10 Ma (Fig. 9a). The predicted lower exhumation rates since the Serravallian are also evident in the exhumation pattern of sample 15M57 from the western footwall of the Büyük Menderes detachment. The thermochronological ages of this sample can be fitted with a continuous exhumation model, which is primarily an effect of the large AFT error (±3.3 Ma). Although the best model predicts an AFT age of 7.5 Ma within error of the observed age (10.6 ± 3.3 Ma), there is evidence from sample 16M97 that the correct AFT age is *c.* 10 Ma, as sample 16M97 is located nearby at the same lateral position in the footwall and yields an AFT age of 9.7 ± 2.9 Ma (Fig. 4a). Combining both samples, by calculating the mean AFT age and the standard error, results in an AFT age of 10.2 ± 0.5 Ma. Repeating the inverse thermokinematic modelling of sample 15M57 with this merged AFT age requires a two-step model (best model AFT age is 10.3 Ma) with a transition from high exhumation rates of >0.5 km Ma^{-1} to lower rates of *c.* 0.2 km Ma^{-1} at 13.5 ± 4.9 Ma (Fig. 9b).

In contrast to the middle Miocene activity observed along the Büyük Menderes detachment, the exhumation in the footwall of the Demirhan detachment commenced in the late Miocene. Sample 15M44 requires a three-step exhumation (lowest BIC value, Table 6), with a change from a relatively vaguely constrained time period of increased exhumation rates in the early Miocene, to slow exhumation rates of *c.* 0.25 km Ma^{-1} in the middle Miocene to higher exhumation rates of *c.* 0.4 km Ma^{-1} at *c.* 7 Ma (Figs 9a and 10c). The increase in exhumation is likely associated with the onset of faulting along the Demirhan detachment. This younger phase of higher late Miocene/Pliocene exhumation rates is also described by Wölfler *et al.* (2017) for a group of samples from the southern part of the Aydın range. They derived exhumation rates of 0.7 km Ma^{-1} assuming a 30°C geothermal gradient and 0.4 km Ma^{-1} assuming a 50°C geothermal gradient, which is in accordance with our modelled exhumation rate of 0.4 km Ma^{-1} with a geothermal gradient of *c.* 38°C km^{-1} (Table 6).

The cessation of extension along the Demirhan detachment can be constrained by the onset of exhumation associated with high-angle normal faulting along the Büyük Menderes graben. This is reflected by the onset of fast exhumation, indicated by sample 14M31 from the hanging wall of the Demirhan detachment. Sample 14M31 requires three exhumation steps to fit the thermochronological data (Table 6). The older time step, at which exhumation rates changed from *c.* 0.6 to *c.* 0.3 km Ma^{-1} is roughly constrained to be in the Oligocene to early Miocene (Fig. 9a). For this time period, a possible extensional reactivation of the basal thrust of the Lycian nappes has been proposed (Ring *et al.* 2003; van Hinsbergen 2010). At 2.9 ± 0.6 Ma, exhumation rates increase to 1.0 ± 0.2 km Ma^{-1} (Table 6). We interpret this increase to be related to the onset of high-angle normal faulting along the northern part of the Büyük Menderes graben, which simultaneously marks the cessation of faulting along the Demirhan detachment. Note that there is a trade-off between exhumation rate and the onset time of faster exhumation (Fig. 9c), i.e. a more recent onset would require higher exhumation rates and vice versa.

The slip rate of the Demirhan detachment

There are two widely used approaches to derive the total slip rate accommodated along low-angle detachments from thermochronological data: (1) plotting the decrease of cooling ages in the down-dip direction of the footwall v. the distance between the samples in the direction of tectonic transport (e.g. Foster & John 1999; Brady 2002; Stockli 2005; Brichau *et al.* 2006; Buscher *et al.* 2013; Singleton *et al.* 2014); and (2) deriving the total slip rate by simple trigonometry from vertical exhumation rates of the footwall (e.g. Schultz *et al.* 2017). The first approach is based on the assumptions that the isotherms have been stable and subhorizontal, that the orientation of the fault did not change and that exhumation was solely caused by tectonic denudation. We also note that the AFT samples should have the same annealing kinetics, and hence similar effective closure temperatures. This is supported for our samples by consistent Dpar values of 1.36 to 1.53 µm, reflecting typical flourine–apatite composition, and the uniform cooling history. The second approach requires one to estimate the original dip angle at which the fault was active. The thermochronological dataset presented in this study and by Wölfler *et al.* (2017) allow us to apply both approaches to constrain the slip rate of the Demirhan detachment.

Firstly, the AFT age of sample 15M44 is combined with four AFT samples from Wölfler *et al.* (2017), which together show decreasing cooling ages in the down-dip direction of the detachment (Fig. 11). A linear regression of the data with *Isoplot* (Ludwig 2003) gives an error-weighted slip rate of 2.6 ± 2.1 (1σ) km Ma^{-1} (or mm a^{-1}) (Fig. 11). The uncertainty of the slip rate is mainly caused by the large errors in the AFT ages. Secondly, based on a modelled exhumation rate of 0.42 ± 0.17 km Ma^{-1} for the samples in the footwall of the Demirhan detachment (sample 15M44, Fig. 9a) and present-day dip of *c.* 15° of the detachment, we calculate a slip rate of 1.6 ± 0.65 km Ma^{-1}. For a steeper dip of 30°, the resulting slip rate

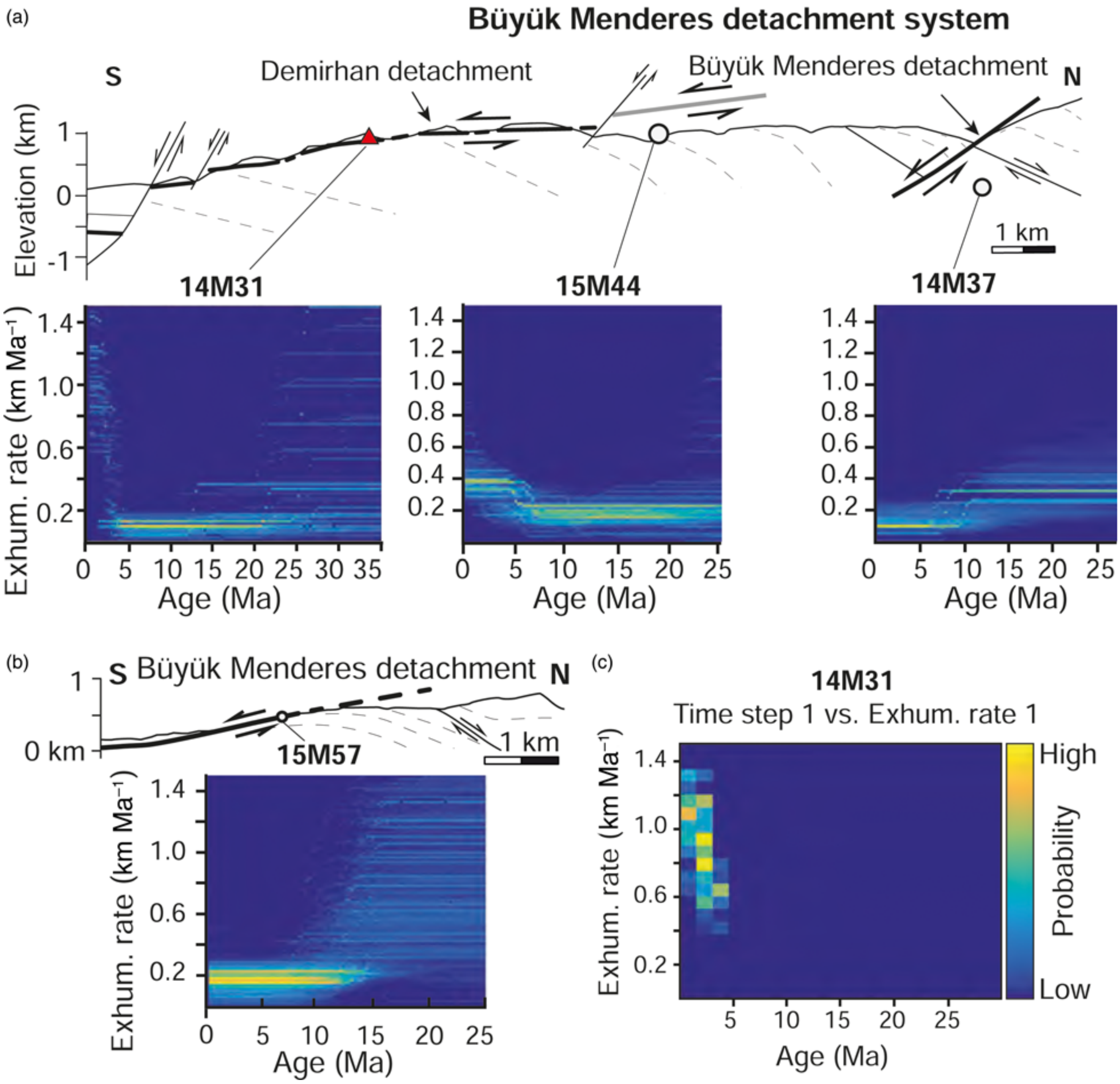

Fig. 9. (**a**) Modelled exhumation rates for the eastern part of the footwall of the Büyük Menderes detachment (14M37) and the Demirhan detachment footwall (15M44) and hanging wall (14M31). (**b**) Modelled exhumation rate for sample 15M57 from the western part of the Büyük Menderes detachment. (**c**) Two-dimensional probability density function showing the linear relationship between T_1 and E_1 of sample 14M31 (exhumation rate for the time between 0 Ma and T_1).

would be 0.8 ± 0.34 km Ma^{-1}. Although both approaches (to determine the slip rate) are associated with high uncertainties, they constrain the slip rate of the Demirhan detachment to be *c.* 2 km Ma^{-1}, which is about half the rate obtained for the Gediz detachment during the same period (4.3 (+3.0/−1.2) km Ma^{-1}; Buscher *et al.* 2013). Considering that faulting along the Demirhan detachment started between the modelled inception at *c.* 7 Ma (Table 6, sample 15M44) and 6 Ma (AFT age of sample 15M44) until its cessation at *c.* 3 Ma, indicated by the onset of high-angle graben faulting at the northern rim of the Büyük Menderes graben, the total displacement along the footwall of the Demirhan detachment is in the order of *c.* 6–*c.* 8 km.

Tectonic implications for the extensional history of the Aydın range

Based on exhumation histories (derived from thermokinematic modelling) and new field observations, we propose a new tectonic model for the Miocene to Recent extensional history of the Aydın range and the evolution of the Büyük Menderes graben (Figs 1 and 2).

The timing of initiation of the extensional tectonic regime, leading to the formation of the central Menderes Massif and the east–west-striking basins, is an ongoing discussion and centres around the question of whether the extension commenced in the early to middle Miocene (Bozkurt 2001) or in the latest Miocene/Pliocene (Gürer *et al.* 2009; Ring *et al.* 2017). For the Bozdağ range, the initiation of detachment faulting along the Gediz detachment is well constrained by the U–Pb intrusion ages of the syntectonic Salihli and Turgutlu granodiorites of *c.* 15 to *c.* 16 Ma, respectively (Glodny & Hetzel 2007). This approach cannot be applied in the Aydın range due to the lack of syntectonic intrusions along the Büyük Menderes detachment. Therefore, most studies inferred the onset of north–south extensional faulting and graben formation indirectly by constraining the depositional ages of the syntectonic Neogene sediments in the Büyük Menderes graben (e.g. Sözbilir & Emre 1990; Seyitoğlu & Scott 1991; Cohen *et al.* 1995). The

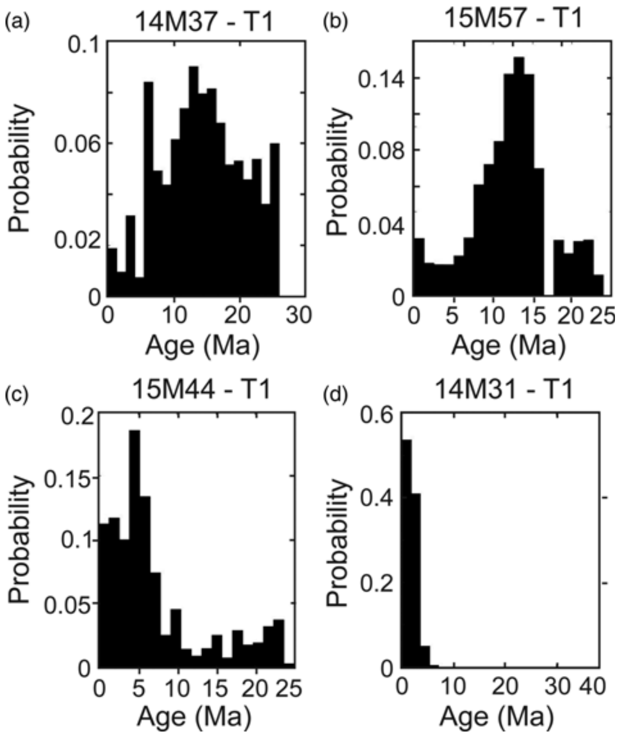

Fig. 10. PDFs (probability density functions) of parameter T_1 (time at which the exhumation rate is changed): (**a**) parameter T_1 of sample 14M37 indicates a middle Miocene change in exhumation rates; (**b**) similarly to the T_1 of 14M37, parameter T_1 of sample 15M57 shows a middle Miocene age; (**c**) sample 15M44 indicates a change from slow to high exhumation rates initiated during the late Miocene; (**d**) sample 14M31 shows the latest Miocene/Pliocene change from slow to high exhumation rates.

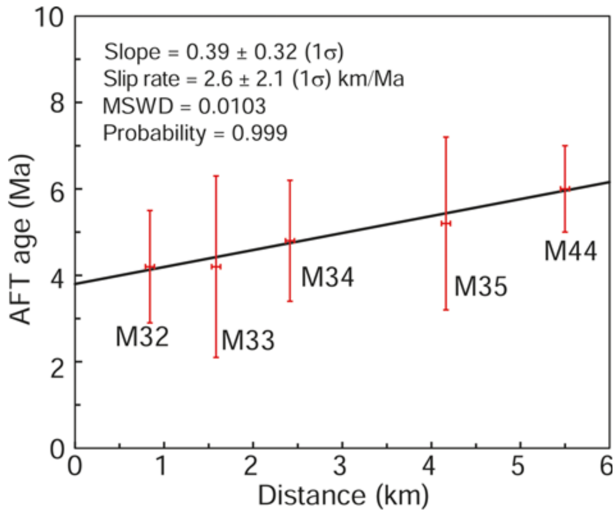

Fig. 11. Slip rate derived from AFT ages (1σ errors) in the footwall of the Demirhan detachment, plotted against distance in slip direction. The observed scatter of the data points from the best-fit line is given as MSWD (mean square of weighted deviates).

difficulty of this approach is the uncertain age of the oldest sedimentary unit, the Hasköy formation.

The depositional ages of the Hasköy formation are either based on palynological dating, yielding ages from early Miocene to late Miocene (Sözbilir & Emre 1990; Seyitoğlu & Scott 1991; Cohen *et al.* 1995; Akgün & Akyol 1999), or on the palaeomagnetic data of Sen & Seyitoğlu (2009) who tentatively suggest a 16–15 Ma depositional age for the Hasköy formation. Alternatively, Gürer *et al.* (2009) proposed that the Hasköy formation was deposited during the formation of the NE- and NW-trending basins in the northern and southern Menderes submassifs, which are inferred to result from a north–south-oriented contractional tectonic regime during the Miocene until the late Pliocene. However, this interpretation is not supported by our thermochronological and structural data, which demonstrate a persistent north–south-directed extension since the Miocene and do not comply with seismic reflection profiles of the Gediz and Büyük Menderes graben, which showed that the Miocene units in both basins were deposited in an extensional half-graben setting (Çiftçi & Bozkurt 2010; Çiftçi *et al.* 2011). Early Miocene (*c.* 22–20 Ma) K–Ar ages for a cataclasite of the Büyük Menderes detachment footwall and for a normal fault in the hanging wall of the detachment, may date the onset of normal faulting in the Aydın range (Hetzel *et al.* 2013).

The first stage of enhanced early to middle Miocene exhumation in the Aydın range was proposed by Wölfler *et al.* (2017) and is corroborated by the additional thermochronological data obtained in this study. Within the context of our new structural model for the Aydın range, almost all samples situated in the footwall of the Büyük Menderes detachment show fast early to middle Miocene exhumation rates of 0.5 ± 0.3 to 0.8 ± 0.4 km Ma^{-1} between the ZHe (mean ZHe ages: 14.9 Ma) and AFT (mean AFT ages: 12.9 Ma) systems (Fig. 10a). However, this exhumation phase is not seen in samples from the footwall of the Demirhan detachment due to their position in the hanging wall of the Büyük Menderes detachment at this time. The relatively large errors associated with the AFT ages prevent resolving the timing of fast exhumation rates during the first stage exhumation event in the middle Miocene by thermokinematic modelling. However, the samples from the eastern part of the Büyük Menderes detachment show fast cooling between *c.* 16 and *c.* 13 Ma (Fig. 6) and samples from the western part show a similar timing with fast cooling occurring at *c.* 13 Ma (Fig. 4a). The middle Miocene activity along the Büyük Menderes detachment coincides with some major tectonic changes in the Aegean and western Turkey, due to the lithospheric response to an accelerated southward roll-back of the Aegean slab commencing at *c.* 15 Ma (e.g. Menant *et al.* 2016). In western Turkey, this is expressed by a southward movement of volcanism and an associated shift to more asthenosphere-derived melts due to the position of western Anatolia above the eastern edge of the Aegean slab (Prelević *et al.* 2012; Menant *et al.* 2016). The extensional processes in western Anatolia are marked by the cessation of detachment faulting along the Simav detachment (Ring & Collins 2005) and the onset of high-angle normal faulting at 17 to 16 Ma (Hetzel *et al.* 2013). Subsequently, the exhumation of the Bozdağ range by the initiation of faulting along the Gediz detachment commences at *c.* 14.5 Ma (Rossetti *et al.* 2017) after the intrusion of granodiorites at 15 and 16 Ma (Glodny & Hetzel 2007). For this early stage movement on the Gediz detachment, Rossetti *et al.* (2017) calculated a cooling rate of *c.* 100°C km^{-1} between 14 and 12 Ma, which is followed by an interval of slow cooling (*c.* 13°C km^{-1}) before a second stage of fast cooling with rates of *c.* 100°C km^{-1} in the latest Miocene/Pliocene. Compared to the Aydın range, the cooling rates in the Bozdağ range are higher, but the similar timing indicates a synchronous activity of the Gediz and the Büyük Menderes detachments during the middle Miocene.

The second exhumation stage in the latest Miocene marks the initiation of faulting along the Demirhan detachment in the Aydın range (Fig. 12b) and the concurrent activity of the Gediz detachment in the Bozdağ range since the Pliocene (Buscher *et al.* 2013). The middle Miocene cooling ages from AFT and 10–7 Ma cooling ages from AHe (Fig. 6) indicate that the footwall rocks of the Büyük Menderes detachment were already close to the surface when faulting along the Demirhan detachment initiated in the latest

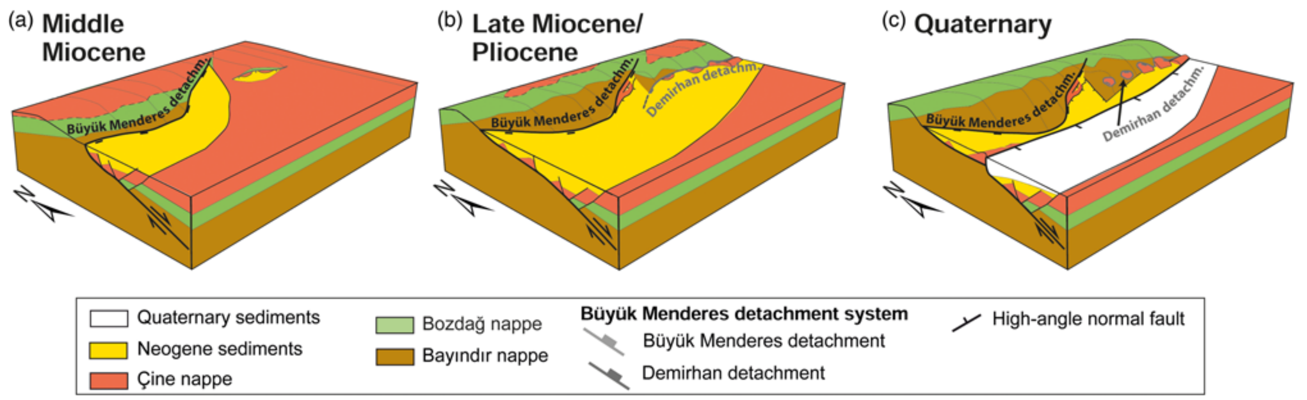

Fig. 12. Sketch illustrating the proposed extensional history of the Aydın range since the middle Miocene. (**a**) Exhumation of the Aydın range in the footwall of the Büyük Menderes detachment and probably early graben formation in the eastern parts of the Büyük Menderes graben. (**b**) Main proportion of extension is accommodated along the Demirhan detachment which exhumes the eastern part of the Aydın range. (**c**) Onset of high-angle normal faulting along the modern graben-bounding fault of the Büyük Menderes graben and uplift and erosion of the Neogene sediments in its footwall.

Miocene (Fig. 9a and Table 6). With a slip rate of about 2 km Ma^{-1}, the Demirhan detachment likely accommodated most of the extension along the southern boundary of the central Menderes Massif but young K–Ar fault gouge ages of *c.* 3–5 Ma indicate that the Büyük Menderes detachment remained active until the Pliocene (Hetzel *et al.* 2013). The inception of faulting along the Demirhan detachment goes along with a widespread tectonic reorganization in the Aegean region and western Turkey, which was caused by the westward propagation of the North Anatolian fault into the Aegean domain (Şengör *et al.* 2005) and the segmentation of the Hellenic slab by the development of a slab tear below the Corinth rift (Royden & Papanikolaou 2011; Jolivet *et al.* 2013). Since the separation from the western part of the Hellenic slab at 5 Ma ago, the trench retreat of the central part of the Hellenic slab accelerated from *c.* 1.7 cm a^{-1} to *c.* 3.2 cm a^{-1} (Brun *et al.* 2017*a*, *b*). Whether the westward propagation of the North Anatolian fault and the associated westward extrusion of Anatolia was caused by the increasing slab retreat rate or by the ongoing continental collision between Arabia and Anatolia is still disputed. In any case, faulting on this strike-slip fault in the Aegean domain is associated with the redistribution of extensional strain from the central Aegean towards the western (Evvia island and Corinth region) and eastern edges (western Anatolia) of the Aegean domain (Royden & Papanikolaou 2011; Menant *et al.* 2016). This new tectonic situation may have favoured the abandonment of the perennial Büyük Menderes detachment and the formation of the new Demirhan detachment in the hanging wall. This is a process that has also been reported from other persistent extensional detachment systems, for example along the North Cycladic Detachment System (NCDS), which accommodated its total amount of extension of 70–90 km in three successively active detachments between 30 and 9 Ma (Jolivet *et al.* 2010). However, compared to the NCDS, the Büyük Menderes detachment system accommodated less extension and most probably does not have a crustal scale pre-extensional precursor, such as the Vardar suture zone for the NCDS. Both systems show that long-lived extensional structures may become ineffective over time. The position of the Demirhan detachment, which occurs not only in the hanging wall but also to the SE of the Büyük Menderes detachment, further implies an eastward propagation of extensional structures with time.

Ongoing extension led to the formation of high-angle normal faults, which bound the modern Büyük Menderes graben to the north and cut the Büyük Menderes and Demirhan detachments. These steeper normal faults must have developed after the activity of the detachments had ceased (Fig. 12c). AHe ages in the footwall of the northern graben-bounding fault range from 2.7 to 0.5 Ma and suggest a late Pliocene to Pleistocene onset of faulting. This is also supported by the thermal modelling results for sample 14M31, which belongs to the hanging wall of the Demirhan detachment and was exhumed in the footwall of the high-angle normal fault (Fig. 9a). Contemporaneously, the Pliocene–Pleistocene Asartepe formation was discordantly deposited above the middle Miocene Gökkırantepe formation during the Pliocene to Pleistocene in the Büyük Menderes graben (Ünay *et al.* 1995; Sarıca 2000). This sedimentary succession is currently uplifted and exposed in the footwall of Quaternary high-angle normal faults whose activity was demonstrated by the surface-rupturing earthquake near Aydın in 1899 (e.g. Altunel 1999). These high-angle normal faults appear to root into a sub-horizontal southward-dipping reflector, which has been interpreted as an active low-angle normal fault at *c.* 2.5 km depth (Çiftçi *et al.* 2011) that accommodates a proportion of the present-day extension rate of 20 mm a^{-1} in western Anatolia (Aktug *et al.* 2009).

Conclusions

The new structural and thermochronological data presented in this study allow a comprehensive interpretation of the extensional history of the Aydın range, and an evaluation of the bivergent exhumation of the central Menderes Massif. Structural mapping of extensional structures demonstrates that extension and exhumation of the Aydın range was not accomplished by slip on a single extensional detachment fault but occurred by faulting on two individual low-angle detachment faults – the Büyük Menderes detachment and the Demirhan detachment in its hanging wall. New thermochronological data shed light on the temporal sequence of the activity of the individual detachments and show that the Büyük Menderes detachment was active in the early to middle Miocene. In the latest Miocene, active detachment faulting started on the Demirhan detachment (although the western part of the Büyük Menderes detachment remained active) and continued until the onset of high-angle normal faulting along the modern Büyük Menderes graben in the Quaternary. Thermokinematic modelling reveals that the footwalls of the Büyük Menderes and Demirhan detachments were exhumed at rates of 0.5 and *c.* 0.4 km Ma^{-1}, respectively. Our results support contemporaneous exhumation of the Aydın and Bozdağ ranges during the middle Miocene and latest Miocene/Pliocene.

Acknowledgements The helpful and constructive comments by an anonymous reviewer, Laurent Jolivet and the careful editorial handling of Yanni Gunnell greatly improved the first version of the manuscript. We thank the inhabitants of the Aydın region for their hospitality and numerous çays.

Funding Funding of this work was provided by grants of the Deutsche Forschungsgemeinschaft (DFG) to C. Glotzbach (GL 724/7-1) and R. Hetzel (HE 1704/18-1) and by the Leibniz Universität Hannover (start-up funds to A. Hampel).

Scientific editing by Yanni Gunnell

References

Akgün, F. & Akyol, E. 1999. Palynostratigraphy of the coal-bearing Neogene deposits graben in Büyük Menderes Western Anatolia. *Geobios*, **32**, 367–383, https://doi.org/10.1016/S0016-6995(99)80013-8

Aktug, B., Nocquet, J.M. *et al.* 2009. Deformation of western Turkey from a combination of permanent and campaign GPS data: Limits to block-like behavior. *Journal of Geophysical Research*, **114**, https://doi.org/10.1029/2008JB006000

Altunel, E. 1999. Geological and geomorphological observations in relation to the 20 September 1899 Menderes earthquake, western Turkey. *Journal of the Geological Society*, *London,* **156**, 241–246, https://doi.org/10.1144/gsjgs.156.2.0241

Asti, R., Malusà, M.G. & Faccenna, C. 2018. Supradetachment basin evolution unravelled by detrital apatite fission track analysis: the Gediz Graben (Menderes Massif, Western Turkey). *Basin Research*, **30**, 502–521, https://doi.org/10.1111/bre.12262

Bozkurt, E. 2000. Timing of extension on the Büyük Menderes Graben, western Turkey, and its tectonic implications. *In*: Bozkurt, E., Winchester, J. A. & Piper, J.D.A. (eds) *Tectonics and Magmatism in Turkey and its Surrounding Area*. Geological Society, London, Special Publications, **173**, 385–403, https://doi.org/10.1144/GSL.SP.2000.173.01.18

Bozkurt, E. 2001. Late Alpine evolution of the central Menderes Massif, western Turkey. *International Journal of Earth Sciences*, **89**, 728–744, https://doi.org/10.1007/s005310000141

Bozkurt, E. & Sözbilir, H. 2004. Tectonic evolution of the Gediz Graben: field evidence for an episodic, two-stage extension in western Turkey. *Geological Magazine*, **141**, 63–79, https://doi.org/10.1017/S0016756803008379

Bozkurt, E., Park, R.G. & Winchester, J.A. 1993. Evidence against the core/cover interpretation of the southern sector of the Menderes Massif, west Turkey. *Terra Nova*, **5**, 445–451, https://doi.org/10.1111/j.1365-3121.1993.tb00282.x

Bozkurt, E., Winchester, J.A. & Park, R.G. 1995. Geochemistry and tectonic significance of augen gneisses from the southern Menderes Massif (West Turkey). *Geological Magazine*, **132**, 287–301, https://doi.org/10.1017/S0016756800013613

Brady, R.J. 2002. Very high slip rates on continental extensional faults: new evidence from (U–Th)/He thermochronometry of the Buckskin Mountains, Arizona. *Earth and Planetary Science Letters*, **197**, 95–104, https://doi.org/10.1016/S0012-821X(02)00460-0

Braun, J. 2003. Pecube: A new finite-element code to solve the 3D heat transport equation including the effects of a time-varying, finite amplitude surface topography. *Computers & Geosciences*, **29**, 787–794, https://doi.org/10.1016/S0098-3004(03)00052-9

Braun, J., van der Beek, P. *et al.* 2012. Quantifying rates of landscape evolu-tion and tectonic processes by thermochronology and numerical modeling of crustalheat transport using PECUBE. *Tectonophysics*, **524–525**, 1–28, https://doi.org/10.1016/j.tecto.2011.12.035

Brichau, S., Ring, U., Ketcham, R.A., Carter, A., Stockli, D. & Brunel, M. 2006. Constraining the long-term evolution of the slip rate for a major extensional fault system in the central Aegean, Greece, using thermochronology. *Earth and Planetary Science Letters*, **241**, 293–306, https://doi.org/10.1016/j.epsl.2005.09.065

Brun, J.P., Sokoutis, D., Tirel, C., Gueydan, F., Van den Driessche, J. & Beslier, M.O. 2017*a*. Crustal versus mantle core complexes. *Tectonophysics*, **746**, 22–45, https://doi.org/10.1016/j.tecto.2017.09.017

Brun, J.P., Faccenna, C., Gueydan, F., Sokoutis, D., Philippon, M., Kydonakis, K. & Gorini, C. 2017*b*. Effects of slab rollback acceleration on Aegean extension. *Bulletin of the Geological Society of Greece*, **50**, 5–23, https://doi.org/10.12681/bgsg.11697

Burchfiel, B.C., Chen, Z., Hodges, K.V., Yuping, L., Royden, L.H., Changrong, D. & Jiene, X. 1992. *The South Tibetan Detachment System, Himalayan Orogen: extension contemporaneous with and parallel to shortening in a collisional mountain belt*. Geological Society of America, Special Papers, **269**, https://doi.org/10.1130/SPE269-p1eological

Burtner, R., Nigrini, A. & Donelick, R.A. 1994. Thermochronology of Lower Cretaceous source rocks in the Idaho-Wyoming Thrust belt. *American Association of Petroleum Geologists Bulletin*, **78**, 1613–1636.

Buscher, J.T., Hampel, A. *et al.* 2013. Quantifying rates of detachment faulting and erosion in the central Menderes Massif (western Turkey) by thermochronology and cosmogenic ^{10}Be. *Journal of the Geological Society, London*, **170**, 669–683, https://doi.org/10.1144/jgs2012-132

Campani, M., Mancktelow, N., Seward, D., Rolland, Y., Müller, W. & Guerra, I. 2010. Geochronological evidence for continuous exhumation through the ductile–brittle transition along a crustal scale low angle normal fault: Simplon Fault Zone, central Alps. *Tectonics*, **29**, TC3002, https://doi.org/10.1029/2009TC002582

Candan, O., Dora, OÖ, Kun, N., Akal, C. & Koraly, E. 1992. Allochthonous metamorphic units at the southern part of Aydın Mountains, Menderes Massif. *Turkish Association of Petroleum Geologists*, **4**, 93–110.

Candan, O., Dora, OÖ, Oberhänsli, R., Çetinkaplan, M., Partzsch, J.H., Warkus, F.C. & Dürr, S. 2001. Pan-African high-pressure metamorphism in the Precambrian basement of the Menderes Massif, western Anatolia, Turkey. *International Journal of Earth Sciences*, **89**, 793–811, https://doi.org/10.1007/s005310000097

Candan, O., Çetinkaplan, M., Oberhänsli, R., Rimmelé, G. & Akal, C. 2005. Alpine high-P/low-T metamorphism of the Afyon Zone and implications for the metamorphic evolution of Western Anatolia, Turkey. *Lithos*, **84**, 102–124, https://doi.org/10.1016/j.lithos.2005.02.005

Candan, O., Koralay, O.E. *et al.* 2011. Supra-Pan-African unconformity between core and cover series of the Menderes Massif/Turkey and its geological implications. *Precambrian Research*, **184**, 1–23, https://doi.org/10.1016/j.precamres.2010.09.010

Carlson, W.D., Donelick, R.A. & Ketcham, R.A. 1999. Variability of apatite fission-track annealing kinetics: I. Experimental results. *American Mineralogist*, **84**, 1213–1223, https://doi.org/10.2138/am-1999-0901

Catlos, E.J., Baker, C., Sorensen, S.S., Çemen, I. & Hançer, M. 2010. Geochemistry, geochronology, and cathodoluminescence imagery of the Salihli and Turgutlu granites (central Menderes Massif, western Turkey): Implications for Aegean tectonics. *Tectonophysics*, **488**, 110–130, https://doi.org/10.1016/j.tecto.2009.06.001

Çemen, I., Catlos, E.J., Gogus O., Ozerdem, C., 2006. Post-collisional extensional tectonics and exhumation of the Menderes massif in the western Anatolia Extended Terrrane, Turkey. *In*: Dilek, Y. & Pavlis, S. (eds) *Postcollisional Tectonics and Magmatism in the Eastern Mediterranean Region*. Geological Society of America, Special Papers, Boulder, Colorado, **409**, 353–379.

Cenki-Tok, B., Expert, M., Işık, V., Candan, O., Monie, P. & Bruguier, O. 2016. Complete Alpine reworking of the northern Menderes Massif, western Turkey. *International Journal of Earth Sciences*, **105**, 1507–1524, https://doi.org/10.1007/s00531-015-1271-2

Çiftçi, N.B. & Bozkurt, E. 2010. Structural evolution of the Gediz Graben, SW Turkey: temporal and spatial variation of the graben basin. *Basin Research*, **22**, 846–873, https://doi.org/10.1111/j.1365-2117.2009.00438.x

Çiftçi, N.B., Pamukçu, O., Çoruh, C., Çopur, S. & Sözbilir, H. 2011. Shallow and deep structure of a supradetachment basin based on geological, conventional deep seismic reflection sections and gravity data in the Buyuk Menderes Graben, Western Anatolia. *Surveys in Geophysics*, **32**, 271–290, https://doi.org/10.1007/s10712-010-9109-8

Cohen, H.A., Dart, C.J., Akyüz, H.S. & Barka, A. 1995. Syn-rift sedimentation and structural development of the Gediz and Büyük Menderes graben, western Turkey. *Journal of the Geological Society*, *London*, **152**, 629–638, https://doi.org/10.1144/gsjgs.152.4.0629

Danišík, M., McInnes, B.I., Kirkland, C.L., McDonald, B.J., Evans, N.J. & Becker, T. 2017. Seeing is believing: Visualization of He distribution in zircon and implications for thermal history reconstruction on single crystals. *Science Advances*, **3**, e1601121, https://doi.org/10.1126/sciadv.1601121

Dodson, M.H. 1973. Closure temperature in cooling geochronological and petrological systems. *Contributions to Mineralogy and Petrology*, **40**, 259–274, https://doi.org/10.1007/BF00373790

Dunkl, I. 2002. TRAKKEY: a window program for calculation and graphical presentation of fission track data. *Computers & Geosciences*, **28**, 3–12, https://doi.org/10.1016/S0098-3004(01)00024-3

Ehlers, T.A. & Farley, K.A. 2003. Apatite (U–Th)/He thermochronometry: Methods and applications to problems in tectonics and surface processes. *Earth and Planetary Science Letters*, **206**, 1–14, https://doi.org/10.1016/S0012-821X(02)01069-5

Emre, T. & Sözbilir, H. 1997. Field evidence for metamorphic core complex, detachment faulting and accommodation faults in the Gediz and Büyük Menderes Grabens, Western Anatolia. *In:* International Earth Science Colloquium on the Aegean and Surrounding Regions, Proceedings, 1995, **1**, 73–94.

Emre, T. & Sözbilir, H. 2007. Tectonic evolution of the Kiraz Basin, Küçük Menderes Graben: evidence for compression/uplift-related basin formation overprinted by extensional tectonics in west Anatolia. *Turkish Journal of Earth Sciences*, **16**, 441–470.

Erkül, F. 2010. Tectonic significance of synextensional ductile shear zones within the Early Miocene Alaçamdağ granites, northwestern Turkey. *Geological Magazine*, **147**, 611–637, https://doi.org/10.1017/S0016756809990719

Ersoy, E.Y., Akal, C. *et al.* 2017. U–Pb zircon geochronology of the Paleogene–Neogene volcanism in the NW Anatolia: Its implications for the Late Mesozoic–Cenozoic geodynamic evolution of the Aegean. *Tectonophysics*, **717**, 284–301, https://doi.org/10.1016/j.tecto.2017.08.016

Farley, K.A. 2000. Helium diffusion from apatite: General behavior as illustrated by Durango fluorapatite. *Journal of Geophysical Research*, **105**, 2903–2914, https://doi.org/10.1029/1999JB900348

Farley, K.A. 2002. (U–Th)/He dating: techniques, calibrations and applications. *Reviews in Mineralogy & Geochemistry*, **47**, 819–844, https://doi.org/10.2138/rmg.2002.47.18

Farley, K.A., Wolf, R.A. & Silver, L.T. 1996. The effects of long alpha-stopping distances on (U–Th)/He ages. *Geochimica et Cosmochimica Acta*, **60**, 4223–4229, https://doi.org/10.1016/S0016-7037(96)00193-7

Flowers, R.M., Shuster, D.L., Wernicke, B.P. & Farley, K.A. 2007. Radiation damage control on apatite (U–Th)/He dates from the Grand Canyon region, Colorado Plateau. *Geology*, **35**, 447–450, https://doi.org/10.1130/G23471A.1

Flowers, R.M., Ketcham, R.A., Shuster, D.L. & Farley, K.A. 2009. Apatite (U–Th)/He thermochronometry using a radiation damage accumulation and annealing model. *Geochimica et Cosmochimica Acta*, **73**, 2347–2365, https://doi.org/10.1016/j.gca.2009.01.015

Foster, D.A. & John, B.E. 1999. Quantifying tectonic exhumation in an extensional orogen with thermochronology: examples from the southern Basin and Range Province. *In*: Ring, U., Brandon M.T., Lister G.S. & Willett S.D. (eds) *Exhumation Processes: Normal Faulting, Ductile Flow and Erosion*. Geological Society, London, Special Publications, **154**, 343–364, https://doi.org/10.1144/GSL.SP.1999.154.01.16

Gautheron, C., Tassan-Got, L., Barbarand, J. & Pagel, M. 2009. Effect of alpha-damage annealing on apatite (U–Th)/He thermochronology. *Chemical Geology*, **266**, 157–170, https://doi.org/10.1016/j.chemgeo.2009.06.001

Gessner, K., Ring, U., Johnson, C., Hetzel, R., Passchier, C.W. & Güngör, T. 2001*a*. An active bivergent rolling-hinge detachment system: Central Menderes metamorphic core complex in western Turkey. *Geology*, **29**, 611–614, https://doi.org/10.1130/0091-7613(2001)029<0611:AABRHD>2.0.CO;2

Gessner, K., Piazolo, S., Güngör, T., Ring, U., Kröner, A. & Passchier, C.W. 2001*b*. Tectonic significance of deformation patterns in granitoid rocks of the Menderes nappes, Anatolide belt, southwest Turkey. *International Journal of Earth Sciences*, **89**, 766–780, https://doi.org/10.1007/s005310000106

Gessner, K., Ring, U., Passchier, C.W. & Güngör, T. 2001*c*. How to resist subduction: Eocene post-high-pressure emplacement of the Cycladic blueschist unit onto the Menderes nappes, Anatolide belt, western Turkey. *Journal of the Geological Society, London*, **158**, 769–780, https://doi.org/10.1144/jgs.158.5.769

Gessner, K., Collins, A.S., Ring, U. & Güngör, T. 2004. Structural and thermal history of poly-orogenic basement: U–Pb geochronology of granitoid rocks in the southern Menderes Massif, Western Turkey. *Journal of the Geological Society, London*, **161**, 93–101, https://doi.org/10.1144/0016-764902-166

Gessner, K., Gallardo, L.A., Markwitz, V., Ring, U. & Thomson, S.N. 2013. What caused the denudation of the Menderes Massif: Review of crustal evolution, lithosphere structure, and dynamic topography in southwest Turkey. *Gondwana Research*, **24**, 243–274, https://doi.org/10.1016/j.gr.2013.01.005

Gleadow, A.J.W. 1981. Fission-track dating methods: what are the real alternatives? *Nuclear Tracks*, **5**, 3–14, https://doi.org/10.1016/0191-278X(81)90021-4

Gleadow, A.J.W. & Duddy, I.R. 1981. A natural long-term track annealing experiment for apatite. *Nuclear Tracks*, **5**, 169–174, https://doi.org/10.1016/0191-278X(81)90039-1

Glodny, J. & Hetzel, R. 2007. Precise U–Pb ages of syn-extensional Miocene intrusions in the central Menderes Massif, western Turkey. *Geological Magazine*, **144**, 235–246, https://doi.org/10.1017/S0016756806003025

Glotzbach, C., Van Der Beek, P.A. & Spiegel, C. 2011. Episodic exhumation and relief growth in the Mont Blanc massif, Western Alps from numerical modelling of thermochronology data. *Earth and Planetary Science Letters*, **304**, 417–430, https://doi.org/10.1016/j.epsl.2011.02.020

Grasemann, B., Schneider, D.A., Stockli, D.F. & Iglseder, C. 2012. Miocene bivergent crustal extension in the Cyclades (Greece). *Lithosphere*, **4**, 23–39, https://doi.org/10.1130/L164.1

Green, P.F., Duddy, I.R., Gleadow, A.J.W., Tingate, P.R. & Laslett, G.M. 1986. Thermal annealing of fission tracks in apatite 1. A qualitative description. *Chemical Geology*, **59**, 237–253, https://doi.org/10.1016/0168-9622(86)90074-6

Guenthner, W.R., Reiners, P.W., Ketcham, R.A., Nasdala, L. & Giester, G. 2013. Helium diffusion in natural zircon: Radiation damage, anisotropy, and the interpretation of zircon (U–Th)/He thermochronology. *American Journal of Science*, **313**, 145–198, https://doi.org/10.2475/03.2013.01

Gürer, Ö.F., Sarıca-Filoreau, N., Özburan, M., Sangu, E. & Doğan, B. 2009. Progressive development of the Büyük Menderes Graben based on new data, western Turkey. *Geological Magazine*, **146**, 652–673, https://doi.org/10.1017/S0016756809006359

Hasözbek, A., Satır, M., Erdoğan, B., Akay, E. & Siebel, W. 2011. Early Miocene post-collisional magmatism in NW Turkey: geochemical and geochronological constraints. *International Geology Review*, **53**, 1098–1119, https://doi.org/10.1080/00206810903579302

Herman, F., Braun, J., Senden, T.J. & Dunlap, W.J. 2007. (U–Th)/He thermochronometry: Mapping 3D geometry using micro-X-ray tomography and solving the associated production-diffusion equation. *Chemical Geology*, **242**, 126–136, https://doi.org/10.1016/j.chemgeo.2007.03.009

Hetzel, R. & Reischmann, T. 1996. Intrusion of Pan-African gneisses in the southern Menderes massif and the age of cooling after Alpine ductile extensional deformation. *Geological Magazine*, **133**, 565–572, https://doi.org/10.1017/S0016756800007846

Hetzel, R., Ring, U., Akal, C. & Troesch, M. 1995*a*. Miocene NNE-directed extensional unroofing in the Menderes Massif, southwestern Turkey. *Journal of the Geological Society, London*, **152**, 639–654, https://doi.org/10.1144/gsjgs.152.4.0639

Hetzel, R., Passchier, C.W., Ring, U. & Dora, OÖ. 1995*b*. Bivergent extension in orogenic belts: The Menderes Massif (southwestern Turkey). *Geology*, **23**, 455–458, https://doi.org/10.1130/0091-7613(1995)023<0455:BEIOBT>2.3.CO;2

Hetzel, R., Zwingmann, H. *et al.* 2013. Spatiotemporal evolution of brittle normal faulting and fluid infiltration in detachment fault systems: A case study from the Menderes Massif, western Turkey. *Tectonics*, **32**, 1–13, https://doi.org/10.1002/tect.20031

Hourigan, J.K., Reiners, P.W. & Brandon, M.T. 2005. U–Th zonation-dependent alpha-ejection in (U–Th)/He chronometry. *Geochimica et Cosmochimica Acta*, **69**, 3349–3365, https://doi.org/10.1016/j.gca.2005.01.024

Huet, B., Labrousse, L. & Jolivet, L. 2009. Thrust or detachment? Exhumation processes in the Aegean: Insight from a field study on Ios (Cyclades, Greece). *Tectonics*, **28**, TC3007, https://doi.org/10.1029/2008TC002397

Hurford, A.J. & Green, P.F. 1983. The zeta age calibration of fission-track dating. *Chemical Geology*, **1**, 285–317, https://doi.org/10.1016/S0009-2541(83)80026-6

Iglseder, C., Grasemann, B., Rice, A.H.N., Petrakakis, K. & Schneider, D.A. 2011. Miocene south directed low-angle normal fault evolution on Kea Island (West Cycladic Detachment System, Greece). *Tectonics*, **30**, TC4013, https://doi.org/10.1029/2010TC002802

Işik, V. & Tekeli, O. 2001. Late orogenic crustal extension in the northern Menderes massif (western Turkey): Evidences for metamorphic core complex formation. *International Journal of Earth Sciences*, **89**, 757–765, https://doi.org/10.1007/s005310000105

Işik, V., Tekeli, O. & Seyitoğlu, G. 2004. The $^{40}Ar/^{39}Ar$ age of extensional ductile deformation and granitoid intrusion in the northern Menderes core complex: implications for the initiation of extensional tectonics in western Turkey. *Journal of Asian Earth Sciences*, **23**, 555–566, https://doi.org/10.1016/j.jseaes.2003.09.001

Jolivet, L. & Brun, J.-P. 2010. Cenozoic geodynamic evolution of the Aegean. *International Journal of Earth Sciences*, **99**, 109–138, https://doi.org/10.1007/s00531-008-0366-4

Jolivet, L. & Patriat, M. 1999. Ductile extension and the formation of the Aegean Sea. *In*: Durand, B., Jolivet, L., Horváth, F. & Séranne, M. (eds) *The Mediterranean Basins: Tertiary Extension within the Alpine Orogen*. Geological Society,London, Special Publications, **156**, 427–456, https://doi.org/10.1144/GSL.SP.1999.156.01.20

Jolivet, L., Lecomte, E. *et al.* 2010. The North Cycladic Detachment System. *Earth and Planetary Science Letters*, **289**, 87–104, https://doi.org/10.1016/j.epsl.2009.10.032

Jolivet, L., Faccenna, C., Huet, B., Labrousse, L., Le Pourhiet, L., Lacombe, O. *et al.* 2013. Aegean tectonics: Strain localisation, slab tearing and trench retreat. *In*: The Aegean: a natural laboratory for tectonics – *Neotectonics*, **597–598**, 1–33, https://doi.org/10.1016/j.tecto.2012.06.011

Karamanderesi, I.H. & Helvacı, C. 2003. Geology and hydrothermal alteration of the Aydın-Salavatlı Geothermal Field, Western Anatolia, Turkey. *Turkish Journal of Earth Sciences*, **12**, 175–198.

Kaymakci, N., Özçelik, Y., White, S.H. & Van Dijk, P.M. 2009. Tectono-stratigraphy of the Çankırı Basin: late Cretaceous to early Miocene evolution of the Neotethyan suture zone in Turkey. *In*: Van Hinsbergen, D. J. J., Edwards, M. A. & Govers, R. (eds) *Collision and Collapse at the Africa–Arabia–Eurasia Subduction Zone*. Geological Society, London, Special Publications, **311**, 67–106, https://doi.org/10.1144/SP311.3

Ketcham, R.A. 2005. Forward and inverse modeling of low-temperature thermochronometry data. *Reviews in Mineralogy and Geochemistry*, **58**, 275–314, https://doi.org/10.2138/rmg.2005.58.11

Ketcham, R.A., Donelick, R.A. & Carlson, W.D. 1999. Variability of apatite fission-track annealing kinetics: III. Extrapolation to geological time scales. *American Mineralogist*, **84**, 1235–1255, https://doi.org/10.2138/am-1999-0903

Ketcham, R.A., Carter, A., Donelick, R.A., Barbarand, J. & Hurford, A.J. 2007. Improved modeling of fission-track annealing in apatite. *American Mineralogist*, **92**, 799–810, https://doi.org/10.2138/am.2007.2281

Koralay, O.E. 2015. Late Neoproterozoic granulite facies metamorphism in the Menderes Massif, Western Anatolia/Turkey: implication for the assembly of Gondwana. *Geodinamica Acta*, **27**, 244–266, https://doi.org/10.1080/09853111.2015.1014987

Koralay, O.E., Satır, M. & Dora, OÖ. 2001. Geochemical and geochronological evidence for Early Triassic calc-alkaline magmatism in the Menderes Massif, western Turkey. *International Journal of Earth Sciences*, **89**, 822–835, https://doi.org/10.1007/s005310000134

Koralay, O.E., Candan, O., Akal, C., Dora, OÖ, Chen, F., Satır, M. & Oberhänsli, R. 2011. Geology and geochronology of the Pan-African and Triassic metagranitoids in the Menderes Massif, Western Anatolia, Turkey. *Bulletin of the Mineral Research and Exploration*, **142**, 69–121.

Lee, J. & Lister, G.S. 1992. Late Miocene ductile extension and detachment faulting, Mykonos, Greece. *Geology*, **20**, 121–124, https://doi.org/10.1130/0091-7613(1992)020<0121:LMDEAD>2.3.CO;2

Lippolt, H.J., Leitz, M., Wernicke, R.S. & Hagerdon, B. 1994. (Uranium + thorium)/helium dating of apatite: experience with samples from different geochemical environments. *Chemical Geology*, **112**, 179–191, https://doi.org/10.1016/0009-2541(94)90113-9

Lips, A.L.W., Cassard, D., Sözbilir, H., Yilmaz, H. & Wijbrans, J.R. 2001. Multistage exhumation of the Menderes Massif, western Anatolia (Turkey). *International Journal of Earth Sciences*, **89**, 781–792, https://doi.org/10.1007/s005310000101

Lister, G.S. & Davis, G.A. 1989. The origin of metamorphic core complexes and detachment faults formed during Tertiary continental extension in the northern

Colorado River region, USA. *Journal of Structural Geology*, **11**, 65–94, https://doi.org/10.1016/0191-8141(89)90036-9

Lister, G.S., Banga, G. & Feenstra, A. 1984. Metamorphic core complexes of Cordilleran type in the Cyclades, Aegean Sea, Greece. *Geology*, **12**, 221–225, https://doi.org/10.1130/0091-7613(1984)12<221:MCCOCT>2.0.CO;2

Lister, G.S., Etheridge, M.A. & Symonds, P.A. 1986. Detachment faulting and the evolution of passive continental margins. *Geology*, **14**, 246–250, https://doi.org/10.1130/0091-7613(1986)14<246:DFATEO>2.0.CO;2

Loos, S. & Reischmann, T. 1999. The evolution of the southern Menderes Massif in SW Turkey as revealed by zircon dating. *Journal of the Geological Society, London*, **156**, 1021–1030, https://doi.org/10.1144/gsjgs.156.5.1021

Ludwig, K.R. 2003. *User's Manual for Isoplot 3.00 A Geochronological Toolkit for Excel*. Berkeley Geochronological Center, Special Publication No. **4**.

Malavieille, J. 1993. Late orogenic extension in mountain belts: insights from the Basin and Range and the late Paleozoic Variscan belt. *Tectonics*, **12**, 1115–1130, https://doi.org/10.1029/93TC01129

McKenzie, D. 1978. Some remarks on the development of sedimentary basins. *Earth and Planetary Science Letters*, **40**, 25–32, https://doi.org/10.1016/0012-821X(78)90071-7

Menant, A., Jolivet, L. & Vrielynck, B. 2016. Kinematic reconstructions and magmatic evolution illuminating crustal and mantle dynamics of the eastern Mediterranean region since the late Cretaceous. *Tectonophysics*, **675**, 103–140, https://doi.org/10.1016/j.tecto.2016.03.007

Naeser, C.W., 1978. *Fission track dating*, US Geological Survey Open File Report 76–190.

Oberhänsli, R., Candan, O., Dora, OÖ & Dürr, S. 1997. Eclogites within the Menderes Massif/western Turkey. *Lithos*, **41**, 135–150, https://doi.org/10.1016/S0024-4937(97)82009-9

Okay, A.I., Tüysüz, O., 1999. Tethyan sutures of northern Turkey. *In*: Durand, B., Jolivet, L., Horvath, E. & Seranne, M. (eds) *The Mediterranean Basins: Tertiary Extension within the Alpine Orogen. Geological Society, London, Special Publications*, **156**, 475–515, https://doi.org/10.1144/GSL.SP.1999.156.01.22

Oner, Z. & Dilek, Y. 2011. Supradetachment basin evolution during continental extension: the Aegean province of western Anatolia, Turkey. *Geological Society of America Bulletin*, **123**, 2115–2141, https://doi.org/10.1130/B30468.1

Özer, S. & Sözbilir, H. 2003. Presence and tectonic significance of Cretaceous rudist species in the so-called Permo-Carboniferous Göktepe Formation, central Menderes metamorphic massif, western Turkey. *International Journal of Earth Sciences*, **92**, 397–404, https://doi.org/10.1007/s00531-003-0333-z

Prelević, D., Akal, C., Foley, S.F., Romer, R.L., Stracke, A. & Van Den Bogaard, P. 2012. Ultrapotassic mafic rocks as geochemical proxies for post-collisional dynamics of orogenic lithospheric mantle: the case of southwestern Anatolia, Turkey. *Journal of Petrology*, **53**, 1019–1055, https://doi.org/10.1093/petrology/egs008

Rahn, M.K., Brandon, M.T., Batt, G.E. & Garver, J.I. 2004. A zero-damage model for fission-track annealing in zircon. *American Mineralogist*, **89**, 473–484, https://doi.org/10.2138/am-2004-0401

Regnier, J.L., Ring, U., Passchier, C.W., Gessner, K. & Güngör, T. 2003. Contrasting metamorphic evolution of metasedimantary rocks from the Çine and Selimiye nappes in the Anatolide belt, western Turkey. *Journal of Metamorphic Geology*, **21**, 699–721, https://doi.org/10.1046/j.1525-1314.2003.00473.x

Reiners, P.W. 2005. Zircon (U–Th)/He thermochronometry. *Reviews in Mineralogy and Geochemistry*, **58**, 151–179, https://doi.org/10.2138/rmg.2005.58.6

Reiners, P.W. & Brandon, M.T. 2006. Using thermochronology to understand orogenic erosion. *Annual Review of Earth and Planetary Sciences*, **34**, 419–466, https://doi.org/10.1146/annurev.earth.34.031405.125202

Reiners, P.W., Zhou, Z., Ehlers, T.A., Xu, C., Brandon, M.T., Donelick, R.A. & Nicolescu, S. 2003. Post-orogenic evolution of the Dabie Shan, eastern China, from (U–Th)/He and fission track thermochronology. *American Journal of Science*, **303**, 489–518, https://doi.org/10.2475/ajs.303.6.489

Reiners, P.W., Spell, T.I., Nicolescu, S. & Zanetti, K. 2004. Zircon (U–Th)/He thermochronometry: He diffusion and comparisons with $^{40}Ar/^{39}Ar$ dating. *Geochimica et Cosmochimica Acta*, **68**, 1857–1887, https://doi.org/10.1016/j.gca.2003.10.021

Ring, U. & Collins, A.S. 2005. U–Pb SIMS dating of synkinematic granites: timing of core-complex formation in the northern Anatolide belt of western Turkey. *Journal of the Geological Society, London*, **162**, 289–298, https://doi.org/10.1144/0016-764904-016

Ring, U., Gessner, K., Güngör, T. & Passchier, C.S. 1999. The Menderes Massif of western Turkey and the Cycladic Massif in the Aegean – do they really correlate? *Journal of the Geological Society, London*, **156**, 3–6, https://doi.org/10.1144/gsjgs.156.1.0003

Ring, U., Willner, A. & Lackmann, W. 2001. Nappe stacking with different pressure–temperature paths: An example from the Menderes nappes of western Turkey. *American Journal of Science*, **301**, 912–944, https://doi.org/10.2475/ajs.301.10.912

Ring, U., Johnson, C., Hetzel, R. & Gessner, K. 2003. Tectonic denudation of a Late Cretaceous–Tertiary collisional belt: regionally symmetric cooling patterns and their relation to extensional faults in the Anatolide belt of western Turkey. *Geological Magazine*, **140**, 421–441, https://doi.org/10.1017/S0016756803007878

Ring, U., Gessner, K. & Thomson, S. 2017. Variations in fault-slip data and cooling history reveal corridor of heterogeneous backarc extension in the eastern Aegean Sea region. *Tectonophysics*, **700–701**, 108–130, https://doi.org/10.1016/j.tecto.2017.02.013

Rojay, B., Toprak, V., Demirci, C. & Süzen, L. 2005. Plio-Quaternary evolution of the Küçük Menderes Graben Southwestern Anatolia, Turkey. *Geodinamica Acta*, **18**, 317–331, https://doi.org/10.3166/ga.18.317-331

Rossetti, F., Asti, R., Faccenna, C., Gerdes, A., Lucci, F. & Theye, T. 2017. Magmatism and crustal extension: Constraining activation of the ductile shearing along the Gediz detachment, Menderes Massif (western Turkey). *Lithos*, **282**, 145–162, https://doi.org/10.1016/j.lithos.2017.03.003

Royden, L.H. & Papanikolaou, D.J. 2011. Slab segmentation and late Cenozoic disruption of the Hellenic arc. *Geochemistry, Geophysics, Geosystems*, **12**, https://doi.org/10.1029/2010GC003280

Rutte, D., Ratschbacher, L., Schneider, S., Stübner, K., Stearns, M.A., Gulzar, M.A. & Hacker, B.R. 2017. Building the Pamir-Tibetan Plateau—Crustal stacking, extensional collapse, and lateral extrusion in the Central Pamir: 1. Geometry and kinematics. *Tectonics*, **36**, 342–384, https://doi.org/10.1002/2016TC004293

Sambridge, M. 1999*a*. Geophysical inversion with a neighbourhood algorithm—I. Searching a parameter space. *Geophysical Journal International*, **138**, 479–494, https://doi.org/10.1046/j.1365-246X.1999.00876.x

Sambridge, M. 1999*b*. Geophysical inversion with a neighbourhood algorithm—II. Appraising the ensemble. *Geophysical Journal International*, **138**, 727–746, https://doi.org/10.1046/j.1365-246x.1999.00900.x

Sarıca, N. 2000. The Plio-Pleistocene age of Büyük Menderes and Gediz grabens and their tectonic significance on N–S extensional tectonics in West Anatolia: mammalian evidence from the continental deposits. *Geological Journal*, **35**, 1–24, https://doi.org/10.1002/(SICI)1099-1034(200001/03)35:1<1::AID-GJ834>3.0.CO;2-A

Schmidt, A., Pourteau, A., Candan, O. & Oberhänsli, R. 2015. Lu–Hf geochronology on cm-sized garnets using microsampling: New constraints on garnet growth rates and duration of metamorphism during continental collision (Menderes Massif, Turkey). *Earth and Planetary Science Letters*, **432**, 24–35, https://doi.org/10.1016/j.epsl.2015.09.015

Schuiling, R.D. 1962. On petrology, age and evolution of the Menderes Massif, W-Turkey; a rubidium/strontium and oxygen isotope study. *Bulletin of the Institute for Mineral Research and Exploration, Turkey*, **58**, 703–714.

Schultz, M.H., Hodges, K.V., Ehlers, T.A., van Soest, M. & Wartho, J.A. 2017. Thermochronologic constraints on the slip history of the South Tibetan detachment system in the Everest region, southern Tibet. *Earth and Planetary Science Letters*, **459**, 105–117, https://doi.org/10.1016/j.epsl.2016.11.022

Schwarz, G. 1978. Estimating the dimension of a model. *The Annals of Statistics*, **6**, 461–464, https://doi.org/10.1214/aos/1176344136

Sen, S. & Seyitoğlu, G., 2009. Magnetostratigraphy of early-middle Miocene deposits from east–west trending Alaşehir and Büyük Menderes grabens in western Turkey, and its tectonic implications. *In*: van Hinsbergen, D.J.J., Edwards, M.A. & Govers, R. (eds) *Collision and Collapse at the Africa-Arabia-Eurasia Subduction Zone*. Geological Society, London, Special Publications, **311**, 321–342, https://doi.org/10.1144/SP311.13

Şengör, A.M.C. & Yilmaz, Y. 1981. Tethyan evolution of Turkey: a plate tectonic approach. *Tectonophysics*, **75**, 181–241, https://doi.org/10.1016/0040-1951(81)90275-4

Şengör, A.M.C., Tüysüz, O. *et al.* 2005. The North Anatolian fault: A new look. *Annual Review of Earth and Planetary Science*, **33**, 37–112, https://doi.org/10.1146/annurev.earth.32.101802.120415

Seyitoğlu, G. & Scott, B.C. 1991. Late Cenozoic crustal extension and basin formation in west Turkey. *Geological Magazine*, **128**, 155–166, https://doi.org/10.1017/S0016756800018343

Seyitoğlu, G. & Scott, B.C. 1992. The age of the Büyük Menderes graben (west Turkey) and its tectonic implications. *Geological Magazine*, **129**, 239–242, https://doi.org/10.1017/S001675680000830X

Seyitoğlu, G., Tekeli, O., Çemen, I., Şen Ş & Işik, V. 2002. The role of the flexural rotation/rolling hinge model in the tectonic evolution of the Alaşehir graben, western Turkey. *Geological Magazine*, **139**, 15–26, https://doi.org/10.1017/S0016756801005969

Shuster, D.L. & Farley, K.A. 2009. The influence of artificial radiation damage and thermal annealing on helium diffusion kinetics in apatite. *Geochimica et Cosmochimica Acta*, **73**, 183–196, https://doi.org/10.1016/j.gca.2008.10.013

Singleton, J.S., Stockli, D.F., Gans, P.B. & Prior, M.G. 2014. Timing, rate, and magnitude of slip on the Buckskin Rawhide detachment fault, west central Arizona. *Tectonics*, **33**, 1596–1615, https://doi.org/10.1002/2013TC003517

Sözbilir H., Emre, T., 1990. Neogene stratigraphy and structure of the northern rim of the Büyük Menderes graben. *In*: Proceedings of International Earth Science Colloquium on the Aegean Region, **2**, 314–322.

Stockli, D.F. 2005. Application of low-temperature thermochronometry to extensional tectonic settings. *Reviews in Mineralogy and Geochemistry*, **58**, 411–448, https://doi.org/10.2138/rmg.2005.58.16

Tagami, T., Galbraith, R.F., Yamada R., Laslett, G.M., 1998. Revised annealing kinetics of fission tracks in zircon and geological implications. *In*: *Advances in Fission-Track Geochronology*. Springer, Dordrecht, 99–112.

Thiede, R.C. & Ehlers, T.A. 2013. Large spatial and temporal variations in Himalayan denudation. *Earth and Planetary Science Letters*, **371**, 278–293, https://doi.org/10.1016/j.epsl.2013.03.004

Thomson, S.N. & Ring, U. 2006. Thermochronologic evaluation of postcollision extension in the Anatolide orogen, western Turkey. *Tectonics*, **25**, TC3005, https://doi.org/10.1029/2005TC001833

Ünay, E., Göktaş, F., Hakyemez, H.Y., Avşar, M. & Şan, Ö. 1995. Dating the sediments exposed at the northern part of the Büyük Menderes Graben (Turkey) on the basis of Arvicolidae (Rodentia, Mammalia). *Geological Bulletin of Turkey*, **38**, 75–80.

Ustaszewski, K., Kounov, A., Schmid, S.M., Schaltegger, U., Krenn, E., Frank, W. & Fügenschuh, B. 2010. Evolution of the Adria-Europe plate boundary in the northern Dinarides: From continent-continent collision to back-arc extension. *Tectonics*, **29**, TC6017, https://doi.org/10.1029/2010TC002668

Valla, P.G., Herman, F., Van Der Beek, P.A. & Braun, J. 2010. Inversion of thermochronological age-elevation profiles to extract independent estimates of denudation and relief history—I: Theory and conceptual model. *Earth and Planetary Science Letters*, **295**, 511–522, https://doi.org/10.1016/j.epsl.2010.04.033

Van Der Beek, P.A., Valla, P.G., Herman, F., Braun, J., Persano, C., Dobson, K.J. & Labrin, E. 2010. Inversion of thermochronological age–elevation profiles to extract independent estimates of denudation and relief history—II: Application to the French Western Alps. *Earth and Planetary Science Letters*, **296**, 9–22, https://doi.org/10.1016/j.epsl.2010.04.032

van Hinsbergen, D.J. 2010. A key extensional metamorphic complex reviewed and restored: the Menderes Massif of western Turkey. *Earth-Science Reviews*, **102**, 60–76, https://doi.org/10.1016/j.earscirev.2010.05.005

Vanderhaeghe, O., 2004. Structural development of the Naxos migmatite dome *In*: Whitney, D.L., Teyssier, C. & Siddoway, C.S. (eds) *Gneiss Domes in Orogeny.* Geological Society of America Special Papers, **380**, 211–228.

Wagner, G.A. & van den Haute, P. 1992. *Fission-Track Dating*. Kluwer Academic, The Netherlands.

Wernicke, B. 1985. Uniform-sense normal simple shear of the continental lithosphere. *Canadian Journal of Earth Sciences*, **22**, 108–125, https://doi.org/10.1139/e85-009

Wernicke, B. 1992. Cenozoic extensional tectonics of the US Cordillera. *In*: Burchfiel, B.C., Lipman, P.W. & Zoback, M.L. (eds) *The Cordilleran Orogen*. Geological Society of America, Boulder, CO, 553–582, https://doi.org/10.1130/DNAG-GNA-G3.553

Whipp, D.M., Ehlers, T.A., Blythe, A.E., Huntington, K.W., Hodges, K.V. & Burbank, D.W. 2007. Plio-Quaternary exhumation history of the central Nepalese Himalaya: 2. Thermokinematic and thermochronometer age prediction model. *Tectonics*, **26**, https://doi.org/10.1029/2006TC001991

Wolf, R.A., Farley, K.A. & Silver, L.T. 1996. Helium diffusion and low temperature thermochronology of apatite. *Geochimica et Cosmochimica Acta*, **60**, 4231–4240, https://doi.org/10.1016/S0016-7037(96)00192-5

Wolf, R.A., Farley, K.A. & Kass, D.M. 1998. Modeling of the temperature sensitivity of the apatite (U–Th)/He thermochronometer. *Chemical Geology*, **148**, 105–114, https://doi.org/10.1016/S0009-2541(98)00024-2

Wölfler, A., Glotzbach, C. *et al.* 2017. Late Cenozoic cooling history of the central Menderes Massif: Timing of the Büyük Menderes detachment and the relative contribution of normal faulting and erosion to rock exhumation. *Tectonophysics*, **717**, 585–598, https://doi.org/10.1016/j.tecto.2017.07.004

Yal, G.P., Eker, A.M., Cambazoglu, S., Sen O., Akgun, H., 2017. Assessment of the early development work for Kuyucak Geothermal Field, Turkey. *In*: Proceedings, 42nd Workshop on Geothermal Reservoir Engineering, Stanford University, Stanford California, February 13–15.

Zaun, P.E. & Wagner, G.A. 1985. Fission-track stability in zircons under geological conditions. *Nuclear Tracks*, **10**, 303–307.

Zeitler, P.K., Herczeg, A.L., McDougall, I. & Honda, M. 1987. U–Th–He dating of apatite: A potential thermochronometer. *Geochimica et Cosmochimica Acta*, **51**, 2865–2868, https://doi.org/10.1016/0016-7037(87)90164-5